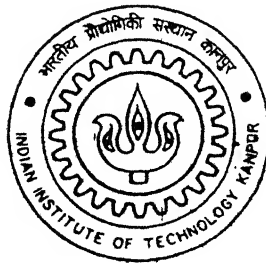


9910526

ENHANCEMENT OF HEAT TRANSFER IN A FIN-TUBE HEAT EXCHANGER USING WINGLETS IN COMMOM FLOW DOWN ARRANGEMENT

By
P. L. N. PRASAD



TH
ME/2001/M
P 886e

DEPARTMENT OF MECHANICAL ENGINEERING
INDIAN INSTITUTE OF TECHNOLOGY KANPUR
AUGUST, 2001

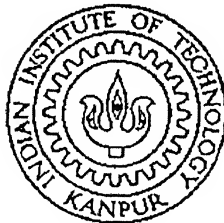
**ENHANCEMENT OF HEAT TRANSFER IN A
FIN-TUBE HEAT EXCHANGER USING WINGLETS
IN COMMOM FLOW DOWN ARRANGEMENT**

*A thesis submitted
in partial fulfillment of the requirements
for the degree of*

MASTER OF TECHNOLOGY

by

P.L.N.PRASAD



**DEPARTMENT OF MECHANICAL ENGINEERING
INDIAN INSTITUTE OF TECHNOLOGY, KANPUR**

August, 2001

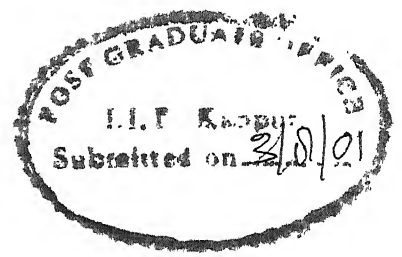
5 FEB 2003 / ME

पुस्तकालय स. विनाथ केनेकर पुस्तकालय
म. वि. वि. नौचोशिकी संस्थान कानपुर

अवधि क्र. A 141969



A141969



Certificate

This is to certify that the thesis entitled “**Enhancement of heat transfer in a fin-tube heat exchanger using winglets in common flow down arrangement**” by Mr. P.L.N.Prasad has been carried out under my supervision. The contents of this thesis have not been submitted to any other Institute or University for the award of any degree or diploma.

Gautam Biswas

Dr. Gautam Biswas

Professor

Department of Mechanical Engineering

Indian Institute of Technology

Kanpur-208016

August 3, 2001

ABSTRACT

Numerical investigation of flow and heat transfer in a rectangular duct with a built-in circular tube in presence of delta-winglet type vortex generators has been carried out for moderate Reynolds numbers and three different angles of attack of the winglets (24° , 30° , 34°). The investigation is necessitated by the need to enhance heat transfer in fin-tube heat exchangers through generation of streamwise longitudinal vortices. The air cooled condenser in geothermal power plants also use fin-tube heat exchangers with circular tubes. The size of these heat exchangers is huge and often the cost of the condenser is more than one-third of the plant cost. Enhancement of heat transfer on the fin surface could reduce the size of the condenser. The strategy for heat transfer enhancement involves introduction of strong swirling motion in the flow field. The swirling motion can be generated by longitudinal vortices. In the present study, the longitudinal vortices have been created by delta winglet type vortex generators with *common-flow-down* configuration. The vortex generators are mounted behind the tubes. An element of heat exchanger has been considered for detailed study of the flow structure and heat transfer analysis. A significant separation delay and removal of zone of poor heat transfer from near-wake of the tubes, culminate as a consequence of employing these vortex generators. The heat transfer in the near wake region can be enhanced as high as 230%. Results also show a marked increase in overall heat transfer in the channel. The enhancement shows a great promise in reducing size of the condensers for geothermal power plants.

ACKNOWLEDGEMENTS

During the journey towards completion of this work, many people have contributed directly or indirectly. I take this opportunity to thank all of them.

I feel very fortunate to have Dr.Gautam Biswas as my thesis supervisor. Without his invaluable suggestions my thesis could have not come to this stage. His amicable personality always gave me pleasure to have discussions with him regarding thesis or any personal matter. I cherish each and every moment I spent with him.

I would like to thank all my colleagues at CFD lab for their help and cooperation. I am thankful to Shaligram, Aseem, Basu, Dalton, Ajay, Srinivas, Ratnesh, Prabhakar, Jawahar and Neetu. Special thanks to Shaligram, Aseem and Dalton for their constant help and encouragement.

But for the constant encouragement of my friends I would not have completed this work. I thank all my friends for bearing me through thick and thin. Special thanks to Narendr, Lachi Ram, Mothi and others.

I shall be always grateful to those invisible persons whose support cannot be expressed in words.

August, 2001

I I T Kanpur

P.L.N.Prasad

CONTENTS

List of figures

Nomenclature

1 Introduction

1.1 Problem Description	1
1.2 The Scope of Present Work.....	3
1.3 Outline of the Thesis.....	3

2 Literature Review

2.1 Introduction.....	5
2.2 Fin-tube Heat Exchangers.....	5
2.3 Numerical Methods for Solving Navier-Stokes Equation.....	10

3 Formulation of the Problem

3.1 Introduction.....	14
3.2 Statement of the Problem.....	14
3.3 Governing Equations.....	16
3.4 Boundary Condition.....	17

4 Grid Generation and Method of Solution

4.1 Introduction.....	19
-----------------------	----

4.2 The Grid.....	19
4.2.1 Grid Generation Technique.....	21
4.2.2 Computational Procedure for Grid Generation.....	22
4.3 Finite Volume Method.....	24
4.4 Surfaces and Volumes.....	25
4.5 Discretization Procedure.....	27
4.5.1 Discretization of Continuity Equation.....	27
4.5.2 Discretization of General Equation.....	28
(a) Rate of Change	28
(b) Convection Fluxes	28
(c) Diffusion Fluxes.....	31
(d) Sources.....	35
4.6 Pressure and Velocity Coupling.....	36
4.7 Solution Algorithm.....	40
4.8 Numerical Stability Considerations.....	45

5 Results and Discussion

5.1 Introduction.....	46
5.2 Flow and Heat Transfer Characteristics in a Rectangular Channel with a built-in Circular Tube.....	46
5.2.1 Flow Characteristics.....	46
5.2.2 Heat Transfer Characteristics.....	52
5.3 Flow Field in Rectangular Channel with a Built-in Circular Tube and Winglet Pair.....	52

5.3.1 Vortex Formation by Winglets.....	56
5.4 Heat Transfer Characteristics in Plane Channel with Built-in Circular Tube and Winglet Pair.....	63
5.5 Influence of Reynolds number and Angle of Attack on Heat Transfer.....	68
5.6 Model Validation.....	68
 6 Conclusion and Scope for future work	
6.1 conclusion.....	72
6.2 Scope for Future Work.....	73
References.....	74

List of Figures

1.1 Schematic diagram of core region of a fin tube heat exchanger.....	2
1.2 Vortex generators on flat fins.....	2
3.1 Computational domain.....	15
4.1 The grid system.....	20
4.2 Three-dimensional finite volume cell.....	26
4.3 Face representation to illustrate diffusion model.....	34
4.4 Iterative solution scheme.....	44
5.1 Streamline plot on horizontal mid-plane.....	47
5.2 Limiting streamline plot on a plane close to the bottom plate.....	48
5.3 Streamline plot on a vertical mid-plane.....	50
5.4 Flow around a cylinder on a flat plate.....	51
5.5 \overline{Nu}_s for plane channel and channel with circular tube.....	53
5.6 Iso-Nusselt number plot on the bottom plate.....	54
5.7 Streamlines on the horizontal mid-plane of the channel.....	55
5.8 Limiting streamlines on a plane close to the bottom plate.....	57
5.9 The wake structure generated by a winglet.....	58
5.10 Vector plot in cross plane at various X locations.....	59
5.11 Flow structure due to delta winglets	61
5.12 Streamline plot in cross plane at various X locations.....	62
5.13 \overline{Nu}_s for channel, channel with circular tube and channel with circular tube and winglet pair.....	64

5.14 Iso-Nusselt number plot on bottom plate.....	66
5.14 (a) Spanwise variation of Nusselt number at $X = 11$	67
(b) Streamlines in cross plane at the same location.....	67
5.15 Variation of \overline{Nu}_s with angle of attack(β).....	69
5.16 Variation of \overline{Nu}_s with the Reynolds number(Re).....	70
5.17 Comparision of local Nusselt number distribution on the tube surface.....	71

NOMENCLATURE

B	Channel width
C_p	Pressure Coefficient, $(p-p_\infty)/\frac{1}{2}\rho u_\infty^2$
cv	Control Volume
D	Diameter of the cylinder
F	Mass flux through a cell face
H	Channel Height
K	Thermal Conductivity
Nu	Local Nusselt number, $(\frac{1}{1-\vartheta_b}) \frac{\partial \vartheta}{\partial z}$
Nu	Span-averaged Nusselt number
p	Static Pressure
P	Grid control Function
Re	Reynolds number based on channel height = $\frac{\rho u_{av} H}{\mu}$
S	Surface area of a cell face
t	Time
u	Axial velocity
v	Spanwise velocity
w	Normal or vertical velocity
x	Axial dimension of coordinates
y	Spanwise dimension of coordinates
z	Normal or vertical dimension of coordinates
T	Temperature

GREEK LETTERS

γ	Upwinding factor
α	Thermal diffusivity
ρ	Density of the fluid
ϑ	Non-dimensional temperature $(T-T_\infty)/(T_w-T_\infty)$
ξ, η	Coordinates in computational space

SUBSCRIPTS

j	Cell face
i	Cell center

SUPERSCRIPTS

n, n+1	Time level
--------	------------

1 INTRODUCTION

1.1 Problem Description

Accomplishment of more efficient heat transfer on the air-side of the air-cooled condensers used in geothermal power plant applications, improves the overall performance of all these plants. The high heat transfer rate must be supported by a modest additional pressure drop across the heat exchangers. One of the efficient means of enhancing heat transfer to achieve high performance of the geothermal air-cooled condensers has been investigated in this work.

In gas-liquid crossflow heat exchangers, fin-tubes are commonly used. In such an arrangement, the gas generally flows across the tubes and the liquid flows inside the tubes. The fins act as extended surfaces providing the bulk of the heat transfer surface area on the air side. Even with the extended surfaces, the dominant thermal resistance is on the air side, since condensation (phase-change heat transfer) takes place inside the tubes. Therefore, in order to achieve significant heat transfer enhancement, strategies must be developed, which result in increased heat transfer coefficients on the fin and the tube outer surfaces without a large increase in pressure drop.

Figure 1.1 shows a schematic diagram of the core region of a fin-tube heat exchanger. Numerical investigations in this field have been carried out by Biswas et al. (1994), where they have tried to achieve the enhancement of heat transfer from the fin surfaces by inducing longitudinal streamwise vortices in the flow field. These vortices were generated with the help of delta-winglet type vortex generators on the flat surface (Figure 1.2). The longitudinal vortices are developed along the side edge of the delta-winglets due to pressure difference between the front surface facing the flow and the back surface. Such vortices are also called streamwise vortices because they have axes collinear with the flow direction, and once they get developed, they interact with an otherwise a two-dimensional

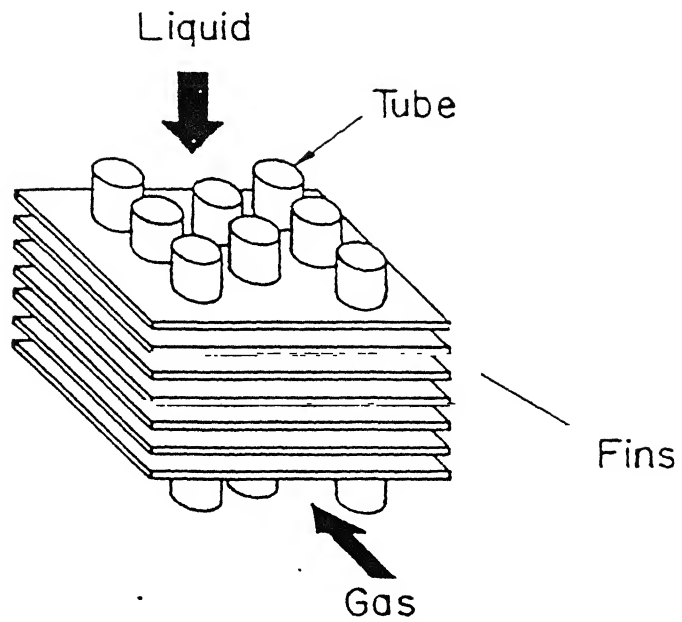


Figure 1.1 Schematic diagram of core region of a fin-tube heat exchanger

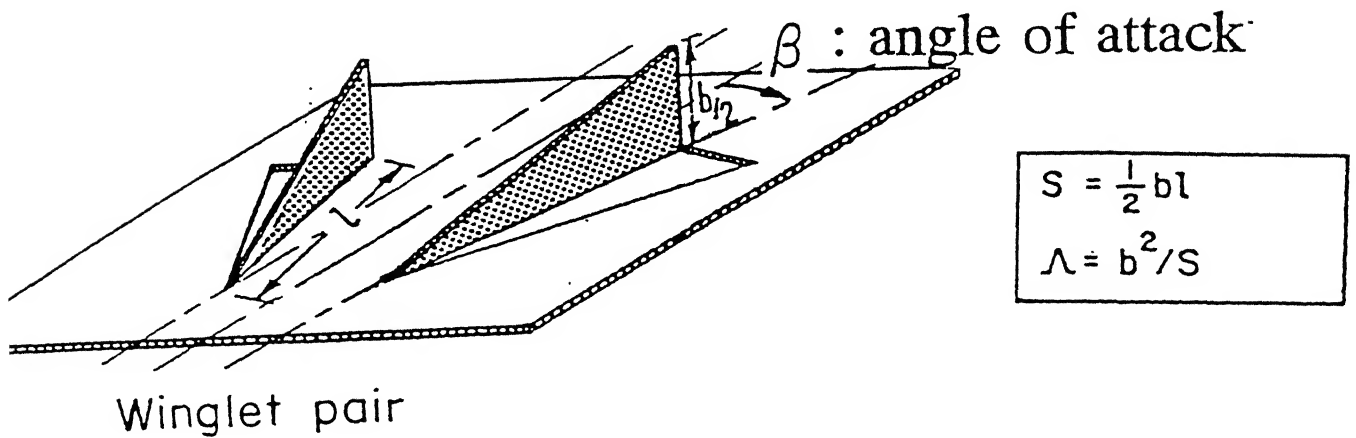


Figure 1.2 Vortex generators on flat fins

boundary layer and produce a three-dimensional swirling flow that mixes near wall fluid with the free stream. This is a type of kinematic mixing and strongly enhances the entrainment of fluid from periphery to the core region of the flow field. It results in disruption of thermal boundary layer which causes enhancement of heat transfer. The additional pressure losses happen to be modest because the form drag for such winglet-type slender bodies is low.

In the present work numerical simulations have been carried out for flow and heat transfer in fin-tube crossflow heat exchangers with delta winglets mounted behind the tube in *common-flow-down* arrangement as proposed by Pauley et al. (1988). The grid-mesh used is of body-fitting type employing finite volume algorithm of Eswaran and Prakash (1998). Figure 1.2 presents a sectional view of the suggested arrangement for fin-tube heat exchangers with delta winglets placed behind in *common-flow-down* configuration.

1.2 The Scope of Present Work

In order to achieve the objective outlined above, a numerical investigation has been carried out. The full Navier-Stokes equations together with the energy equation are solved in a rectangular channel with a built-in circular tube having delta winglets placed in *common-flow-down* configuration in the down stream. A detailed analysis of the flow structure together with heat transfer characteristics in such a module are studied.

1.3 Outline of the Thesis

In Chapter-1 the genesis of the problem has been discussed. Chapter-2 of the thesis provides a review of the literature relevant to understanding of the basic mechanism involved in augmentation of heat transfer and the algorithms related to solving the Navier-Stokes equations. A concise review of modeling aspects of transient flow has also been focussed in Chapter-2. The mathematical formulation of the problem for simulation is presented

in Chapter-3. In this chapter, the flow geometry, the governing equations, boundary conditions and grid generation techniques are discussed. Chapter-4 discusses the solution algorithm and all the basic description of the finite volume formulation in detail. Chapter 5 discusses the results for laminar flow with a detailed study of flow physics and associated heat transfer. Chapter-6 includes the concluding remarks and the scope for further research.

2 LITERATURE REVIEW

2.1 Introduction

Considerable amount of experimental, analytical and computational research has been carried out on enhancement of heat transfer. The enhancement of heat transfer through manipulation of surface geometry has been analyzed by many researchers and practitioners and the concerned literature is presented in this chapter. In order to analyze the flow structure and heat transfer in such applications, a detailed computational study is needed. In such applications, flow regime may possess either laminar or turbulent characteristics. Here important numerical techniques developed in the recent past for solving the conservation equations for complex flows and heat transfer have been focussed. Numerical solutions for laminar flows and heat transfer have been well developed by various researchers but the corresponding investigations for turbulent flows involve more rigorous considerations. Present literature survey helps in suggesting the work to be carried out to achieve the objectives enumerated in Chapter-1. The review of literature follows in two sections, the first presenting an overview of work done by various researchers in the area of enhancement of heat transfer. The second section presents a review of investigations pertaining to the numerical methods with regard to the task of computing flow fields in complex geometries thereby it deals with available scheme for solving complete Navier-Stokes equations.

2.2 Enhancement of Heat Transfer

The primary interest of present work is to enhance the heat transfer in the gas side of fin-tube heat exchangers (with flat fins). With that as aim, we would like to study different investigations related to heat transfer enhancement suitable for the applications proposed above.

Investigation of heat transfer enhancement in channel flows where the rate of heat

transfer between the fluid and channel walls keeps diminishing due to growth of boundary layer as the flow tends to get fully developed, is of special interest. Surface protrusions on the channel walls destabilize hydrodynamic boundary layer and disrupt the thermal boundary layer and thereby enhance the heat transfer between the flowing fluid and channel walls. Applications of such flow configurations are the heat transfer between the gas and the fin in the case of gas-liquid fin-tube cross flow heat exchangers and the heat transfer between the flowing fluid and plates in the case of fin-plate heat exchangers. The use of a multi-layered surface geometry for plates can disturb evolution towards a fully developed flow. A detailed performance data for louvered fin surfaces is provided by Achaichia and Cowell (1988). In using louvered fins, enhancement in heat transfer is obtained at the price of high-pressure drop and so to take care of that, protrusions in the form of slender delta-wings or winglets can be mounted on the fin surfaces (Figure 1.2). As shown, the base of the wing remains attached to the fin and the apex faces the incoming stream with an angle of attack in this configuration.

2.2.1 Vortex Generators

Detailed investigations of the enhancement potential of vortex generators have been carried out in the last two decades (Fiebig et al. (1986), Turk and Junkhan (1986), Eibeck and Eaton (1986), Fiebig et al. (1989), Amon (1989), Dong (1989), Zhang (1989), Tiggelbeck (1992), Yanagihara and Torii (1990), Fiebig et al. (1990), Fiebig et al. (1991), Sanchez (1989), Valencia (1992), Biswas et al. (1994) and Valencia (1996)). The idea of using vortex generators in compact heat exchangers is being used by the industry. Transverse vortex generators, such as ribs and corrugations in channels generate vortices whose axes are mainly transverse to the primary flow direction, whereas, longitudinal vortex generators, such as delta wings and rectangular wings generate vortices having axes mainly along the primary flow direction. The experimental and numerical investigations conducted so

far show that longitudinal vortex generators are preferable to transverse vortex generators for improvement of heat transfer surfaces in the heat exchangers when both heat transfer enhancement and flow loss are taken into account.

The generation of longitudinal vortices along the side edge of the wing-shaped vortex generators appears due to the pressure difference between the front surface facing the flow and the back surface. In a channel, these vortices can be made to disturb the growth of thermal boundary layer by mixing fluid from the near wall region and the channel core region. They can serve to enhance the heat transfer rate while producing less increase in pressure loss penalty. The enhancement in heat transfer is caused by the mixing induced by these vortices, of the mid-stream and the boundary layer fluids which causes steeper temperature gradients to develop near the wall. The application of longitudinal vortices for boundary layer control is well known (Pearcey 1961) and such vortex generators find prominent use in aircraft industry.

The study of streamwise longitudinal vortices behind a slender aerodynamic object is a research topic of much interest for many years. Hummel and Srinivasan (1967) have made important contribution in revealing the complex flow structure behind a delta wing. They have conducted experiments and presented pressure distribution and vortex structure of the flow around a delta wing of unit aspect ratio with an angle of attack of 20° . Fiebig et al. (1986), Fiebig et al. (1991) and Tiggelbeck et al. (1992) have also carried out experimental investigations for augmentation of heat transfer by means of longitudinal vortices. Fiebig et al. (1986) in their experimental study compared the performance of different kinds of vortex generators viz. delta wing, rectangular wing, delta winglet pair and rectangular winglet pair in the Reynolds number of 1360 and 2270. Their observation depicts that the delta wing is the best vortex generator from the heat transfer point of view. Another important feature of their observation is that the heat transfer coefficient increases with the increase in angle of attack till the vortex break down takes place. Tiggelbeck et al.

(1992) used multiple rows of vortex generators in an aligned arrangement within a channel and observed their influence on flow structure. They found that the flow structure in the wake of the second row has similar qualitative characteristics to that of the first row. They also observed that the peak value of the spanwise averaged Nusselt number at the location of the wake of second row is strongly dependent on the spacing between the two rows. Fiebig et al. (1989) and Biswas and Chattopadhyay (1992) carried out computational studies for geometry of delta wing placed inside a channel. They discussed the influence of angle of attack and Reynolds number on velocity and temperature fields in the laminar range.

The gas side heat transfer coefficient in a gas liquid fin-tube heat exchanger is small as compared to that of liquid side. The mechanism of heat transfer between the gas and the solid surface in such cases is to be understood in detail. Consider flow past a tube in a channel with neighboring fins. The emerging flow field consists of a horseshoe vortex system, a dead water zone at the junction of the tube and the plate and a von-Karman vortex street in the middle. To enhance heat transfer in such flow configuration, vortex generators can be mounted on the plates, which make the flow field extremely complex. Experiments conducted by Dong (1989) and Valenica et al. (1996) show the influence of winglet type vortex generators in a channel with a built-in circular tube. Biswas et al. (1994) have observed that in the absence of winglet type vortex generators, relatively little heat transfer takes place in the downstream of the circular tube which is the recirculation region with low velocity. However, they observed an enhancement of heat transfer as high as 240 percent in the wake region behind the cylinder in the presence of winglet type longitudinal vortex generators. Fluid flow and heat transfer characteristics through a parallel plate channel with transverse ribs, which act as vortex generators, have been investigated by Webb and Ramadhyani (1985). Significant heat transfer augmentation is obtained in their study. Acharya et al. (1991) explained vortex interaction between two

such ribs in a channel for the sub-harmonic excitation of shear layers. Even positioning of vortex generators at key locations in the flow has its influence on enhancement of heat transfer (Myrum et al. 1992).

The vortex generators are special surfaces that are used to generate secondary flow or vortices by swirling and destabilizing the flow. In addition, these vortices have a tendency to last for a long period and to have small cores, allowing an influence on heat transfer over long and narrow regions (Fiebig 1998). The vortex generators can generate transverse or longitudinal vortices depending on the geometry and angle of attack of the vortex generators. The axis of transverse vortices (also called spanwise or primary vortices) is perpendicular to the main flow direction. These type of vortices are generated from flow separation and unstable shear layers, and the flow can remain two-dimensional. The Karman vortex street in the wake of bluff bodies, e.g., circular and rectangular cylinders, is one known example of transverse vortices as studied by Sohankar et al. (1999) and Sohankar et al. (2000). Sohankar and Davidson (2001) have numerically investigated the effect of inclined vortex generators on heat transfer enhancement in a three-dimensional channel. They have confirmed that the downwash of the secondary flow induced by vortex generators increases mixing of cold and hot fluid and enhances heat transfer. They also showed that when thicker vortex generators are used stronger and bigger streamwise vortices are formed downstream of the vortex generators which give rise to a higher Nusselt number. Fiebig (1998) concluded that in general, longitudinal vortices are more efficient than transverse vortices for heat transfer enhancement. In addition, longitudinal vortices enhance locally and globally in steady flow, while transverse vortices generate a negligible global heat transfer enhancement in steady flow.

Numerical investigation of convective heat transfer and pressure drop in wavy ducts is carried out by Blomerius and Mitra (2000) in the laminar to transitional range of Reynolds number (600-2000). They have determined the geometrical parameters for the best ratio

of heat transfer to pressure drop for three-dimensional channels consisting of corrugated plates. Both 2-D and 3-D geometries are considered by them where two-dimensional computations show the onset of self-sustained flow oscillation above a critical Reynolds number and an associated enhancement of heat transfer. Two-dimensional parametric studies have been used to identify potentially interesting three-dimensional geometries.

2.3 Numerical Methods for Solving Navier-Stokes Equation

For last three decades various solution techniques have been proposed for full Navier-Stokes equations. The solution techniques for incompressible flows do not have any explicit equation for pressure and so due to spatial coupling of pressure and velocity it becomes quite difficult to obtain direct numerical solutions. Pressure does not have the usual thermodynamical meaning in incompressible flow problems and becomes a relative variable, which adjusts itself instantaneously for the condition of zero mass divergence to be satisfied at all computational cells. The primitive variable formulation of the incompressible Navier-Stokes equations has following most distinctive feature. Because in incompressible Navier-Stokes equations speed of sound is treated to be infinite, the pressure field cannot be calculated by explicit time advancement procedure and so it require at least a partially implicit determination which takes into account the coupling between the pressure and velocity fields as well as the effects of the velocity boundary conditions. This pressure field can be conveniently computed using stream function-vorticity approach for two-dimensional flows but it again creates problem for computation of three-dimensional flows due to absence of single scalar stream function.

Primitive variable approach can be employed for three-dimensional problems which can be followed without encountering non-physical wiggles in pressure distribution. Harlow and Welch (1965) have used a staggered grid for the dependent variables in their well known MAC (Marker and Cell) method which is one of the earliest and widely used explicit

methods for solving the full Navier-Stokes equations. In this method, solution of velocities are obtained using a two step procedure. In the first step called the predictor step, the provisional values of velocity components are computed explicitly using advection, diffusion and pressure gradient of the earlier time steps. This explicitly advanced provisional velocity field may not necessarily ensure a divergence free velocity field. Hence, in the second step called the corrector step, the pressure and velocity components are corrected so that the velocity field satisfies the continuity equation. This is done through the solution of a Poisson equation for pressure. A relative technique, known as pseudo-compressibility method, developed by Chorin (1967) involves a simultaneous iteration of the pressure and velocity components. Vicelli (1971) has shown that the method due to Chorin (1967) and the MAC method are equivalent.

Since implicit methods have no such restrictions, they are more attractive. Patankar and Spalding (1972) have introduced an efficient method known as SIMPLE (Semi-Implicit method for Pressure Linked Equations). This method is based on a finite-volume discretization of the governing equations on a staggered grid. In order to improve the convergence involved in the pressure-velocity coupling, several variants of SIMPLE algorithm have been developed. The SIMPLER algorithm of Patankar (1981) and the SIMPLEC algorithm of Van Doormaal and Raithby (1984) are improvements on SIMPLE. Although the changes to incorporate SIMPLEC into SIMPLE algorithm are minor, the consequences can be as great as it eliminates the approximations made in SIMPLE while deriving the pressure-velocity corrections.

Application of finite volume methods using non-orthogonal coordinates and collocated grids is reported by Rhie and Chow (1983) and Peric (1985). Ferziger and Peric (1999) have shown that collocated arrangement converges faster than the staggered variable arrangement and has advantages when extensions such as multigrid techniques and non-orthogonal grids are considered. Mukhopadyay et al. (1993) has developed a numerical method for

incompressible geometries. Integral mass and momentum conservation equations are discretized into algebraic form through numerical quadrature. The physical domain is divided into a number of non-orthogonal control volumes which are iso-parametrically mapped on to standard rectangular cells. Numerical integration for unsteady momentum equation is performed over such non-orthogonal cells. The results exhibit good accuracy and justify the applicability of the algorithm. Kobayashi and Pereira (1991) have modified the momentum interpolation method suggested by Peric (1985) and named it as Pressure-Weighted Interpolation Method-corrected (PWIMC). In this method, non-orthogonal terms in the momentum equations were solved explicitly, whereas in the pressure-corrections they were dropped. The finite volume algorithm developed by Eswaran and Prakash (1998) for solving time dependent three-dimensional full Navier-Stokes equation has the following advantages:

- It uses collocated grid arrangement, hence all the advantages of collocated grid arrangement are gainfully utilized.
- The essence of the algorithm is SMAC so it is suitable for modeling unsteady flows (see Kim and Benson, 1992).
- The governing equations are discretized in the physical plane itself without coordinate transformation.

This algorithm has been used to solve the flow problem and extended to solve the energy equation for the present work. Peric et al. (1988) carried out a comparative study of finite volume numerical methods with staggered and collocated grids. They concluded that the collocated method possesses no disadvantage relative to the staggered grid version. The treatment of boundary conditions and the implementation of higher order differencing schemes is simpler. In some cases, the collocated version provides faster convergence. It behaves similar to the staggered version under the variation of grid and under-relaxation

parameters, and provides solutions of equal accuracy at the same or lower computing cost.

3 FORMULATION OF THE PROBLEM

3.1 Introduction

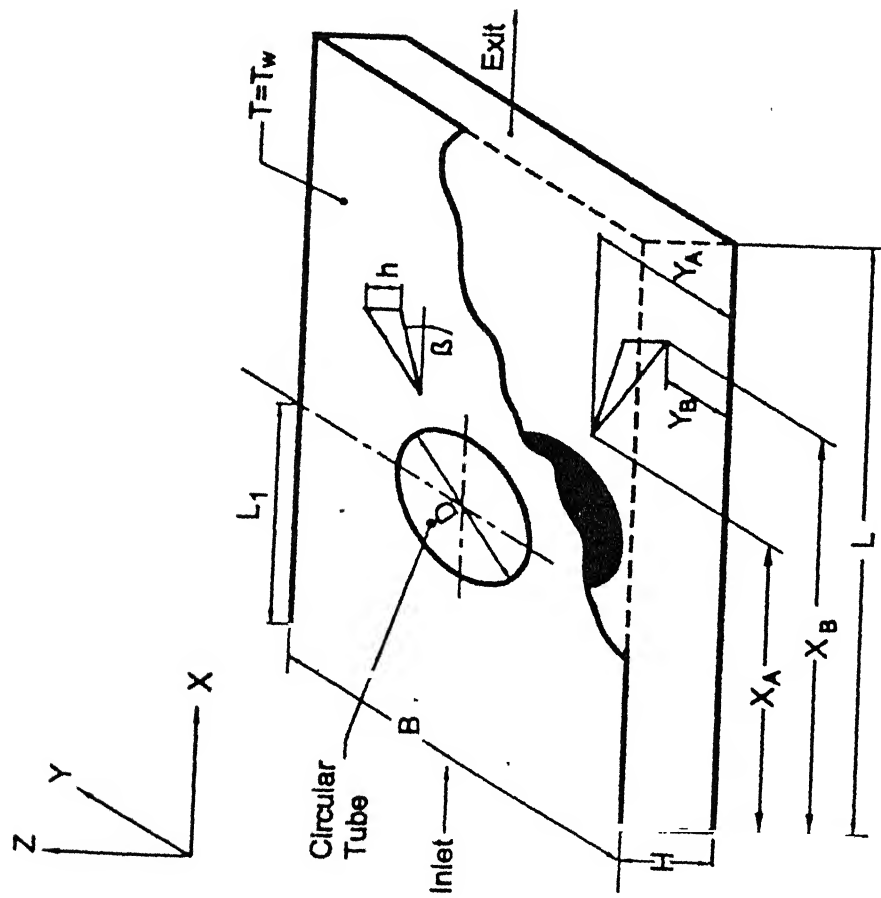
The need to augment the heat transfer in fin-tube heat exchangers so as to reduce their size and thereby cost, has led us to compute the flow and heat transfer characteristics in a horizontal channel with a built-in circular tube and a pair of winglets. This numerical study can provide information about the heat transfer enhancement in fin-tube heat exchangers and effect of various parameters on the transport enhancement.

3.2 Statement of the Problem

The computational domain is shown in Figure 3.1. Two neighboring fins form a channel of height H , width $B = 11.25H$ and length $L = 25H$. The circular tube of diameter $D = 2.8H$ is located at a distance $L_1 = 6.25D$ from the inlet. The blockage ratio, D/B has been kept 0.25. The position of the winglet is $X_A = 7.5H$ and $X_B = 10.5H$, $Y_A = 2.8H$ and $Y_B = 1.125H$, $h = 0.67H$ and angle of attack has been varied. Air has been used as working fluid, hence the Prandtl number of the study is 0.7.

The flow field in the channel with built-in circular tube and a winglet pair is characterized by the following parameters:

- Reynolds number
- Blockage ratio (D/B)
- Position of the cylinder in the channel (L_1/L)
- Velocity profile at the channel inlet
- Channel height (H/B)
- Angle of attack of the winglets (β)



$L = 25$
 $B = 11.25$
 $H = 1$
 $L_1 = 6.25$
 $D = 2.8$
 $X_A = 7.5$
 $X_B = 10.5$
 $Y_A = 3$
 $Y_B = 0.75$
 $h = 0.67$

Figure 3.1 Computational Domain

- Height of the winglets (h/H)
- Position of the winglets (X_A/L , Y_A/L)

3.3 Governing Equations

For laminar flow of an arbitrary spatial control volume V bound by a closed surface S the three-dimensional Navier-Stokes equation can be expressed in the following general convection-diffusion-source integral form:

$$\frac{\partial}{\partial t} \int_V \rho dV + \oint_S \rho \vec{u} \cdot d\vec{S} = 0 \quad (3.1)$$

$$\frac{\partial}{\partial t} \int_V \rho \phi dV + \oint_S (\rho \vec{u} \phi - \Gamma_\phi \nabla \phi) \cdot d\vec{S} = \int_V S_\phi dV \quad (3.2)$$

Where ρ represents the fluid density, \vec{u} is the fluid velocity, ϕ stands for any vector component or scalar quantity, S_ϕ is the volumetric source term. For incompressible flow of Newtonian fluid, the equation becomes

$$\oint_S \vec{u} \cdot d\vec{S} = 0 \quad (3.3)$$

$$\frac{\partial}{\partial t} \int_V \rho \phi dV + \oint_S (\rho \vec{u} \phi - \Gamma_\phi \nabla \phi) \cdot d\vec{S} = \int_V S_\phi dV \quad (3.4)$$

and the source term for momentum equation becomes $-\frac{1}{\rho} \int p I \cdot d\vec{S}$ where I is the unit tensor.

Here we work with Cartesian components of velocity. So ϕ can be the three-Cartesian

components of velocity u , v , and w as well as any scalar e.g., temperature which need to be determined. It is to be noted that Equation (3.2) is a perfectly general equation from which the three fundamental equations of flow and heat transfer (i.e., continuity, momentum and energy) can be derived. The Table 3.1 displays substitutions for ϕ in general transport equation to obtain the conservation equations for mass, momentum and energy. Basu et al. (2001) have computed flow and heat transfer in a cross flow past a circular tube placed in a channel.

Table 3.1: Values of the variables in the general transport Equation (3.2).

Equation	ϕ	Γ_ϕ	S_ϕ
Continuity	1	0	0
Momentum	u_j	μ	$\frac{\partial p}{\partial x_j}$
Energy	T	$\frac{k}{C_P}$	0

3.4 Boundary Conditions

The governing differential equations are elliptic in space and parabolic in time. The boundary conditions for all confining surfaces are required which are outlined below.

- Top and bottom plates

$$u = v = w = 0 \quad (\text{No slip boundary condition}) \text{ and } \frac{\partial p}{\partial z} = 0$$

$$T = T_w \quad (T_w \text{ represents wall temperature})$$

- Side Walls

$$\frac{\partial u}{\partial y} = \frac{\partial w}{\partial y} = 0, \quad v = 0 \quad (\text{Free slip boundary condition}) \text{ and } \frac{\partial p}{\partial y} = 0$$

$$\frac{\partial T}{\partial y} = 0$$

- Channel inlet

$$u = U_{\infty}, \quad v = w = 0 \text{ and } \frac{\partial p}{\partial x} = 0$$

$$T = T_{\infty}$$

- Channel exit

$$\frac{\partial \phi}{\partial t} + U_{av} \frac{\partial \phi}{\partial x} = 0 \quad (\text{Orlanski boundary condition})$$

(where ϕ represents either of u , v , w or T)

$$p = p_{\infty}$$

- Obstacles (Cylinder and Winglet)

$$u = v = w = 0 \text{ and } \frac{\partial p}{\partial n} = 0 \quad (\text{where } n \text{ signifies the normal direction})$$

$$T = T_w$$

4 GRID GENERATION AND METHOD OF SOLUTION

4.1 Introduction

The numerical solution of the governing equations in the prescribed computational domain with given initial and boundary conditions involves two major discretization steps. First being the discretization of the domain with the help of a numerical grid used for computation. The governing equations are discretized on the basis of this numerical grid. Various ways of discretization can be applied to the above set of partial differential equations. Among these the most common methods are those using finite differences, finite elements and finite volumes. In the present work a finite volume scheme is chosen for spatial discretization of the governing equations. As a result, a conservative formulation of the discretization is possible, assuring automatically the satisfaction of the global balance of the conserved quantities, independent of the coarseness of the numerical grid.

4.2 The Grid

Figure 4.1 shows the schematic of the two dimensional grid used in the present work. The grid generation technique uses *block partitioning* method to generate the grid. The whole domain is divided into two blocks. In first block where winglets have been placed, cartesian grid is generated. In the second block where a built-in circular tube is placed, a differential equation technique is used for generation of the body-fitting grid. The two dimensional grid-mesh is stacked in the third direction to obtain the three dimensional grid-mesh. The grid generation technique adopted for body-fitting type is described in brief in the following sections. Three categories of physical domains may exist viz. (1) a simply-connected domain, (2) a doubly-connected domain and (3) a multiply-connected

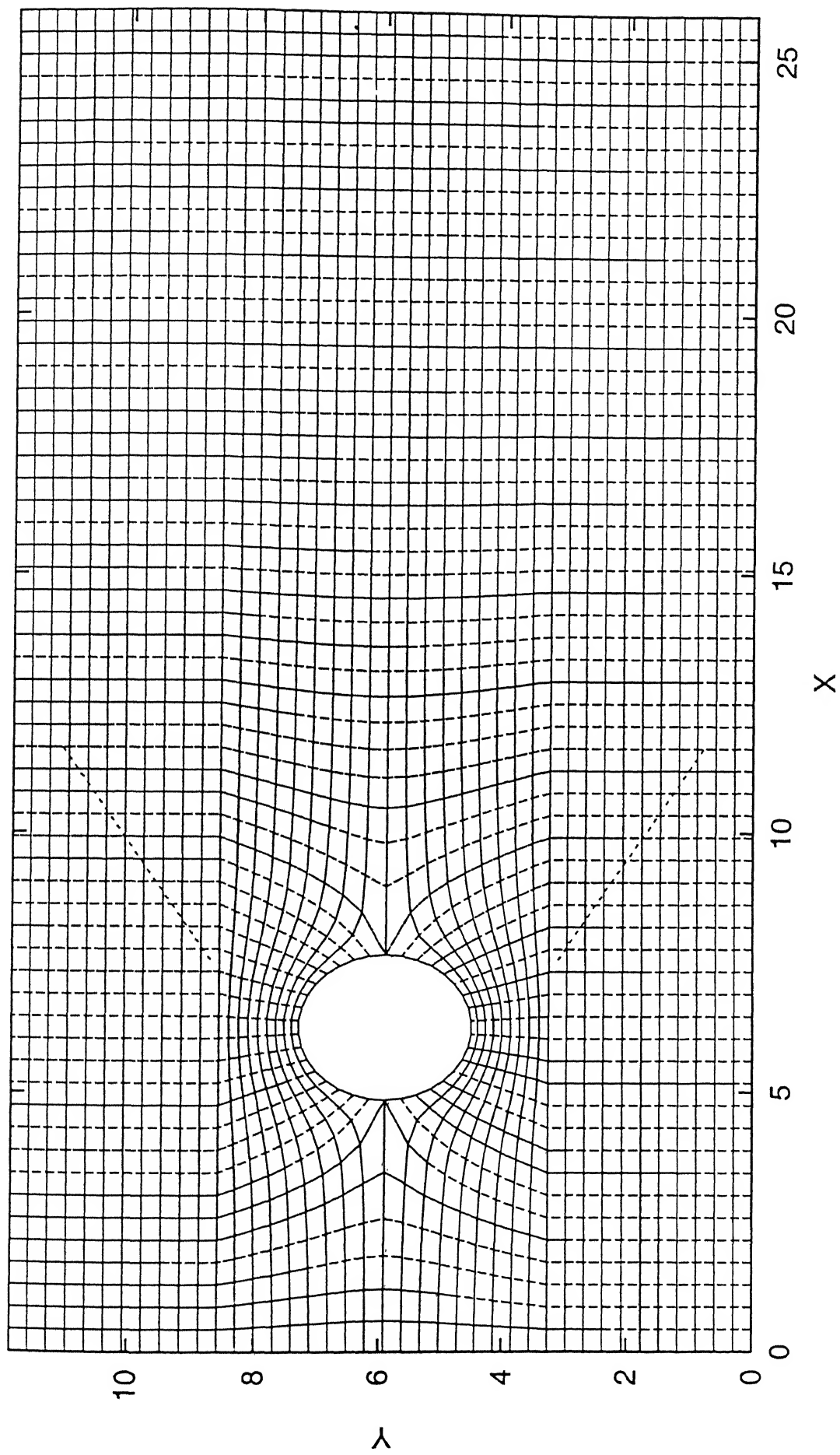


Figure 4.1 The Grid System

domain. Here simply-connected domain is used in the body-fitting region.

4.2.1 Grid Generation Technique

The two-dimensional grid has been generated using tranfinite interpolation and differential equation method. The method of tranfinite interpolation essentially uses linear interpolation scheme to compute the interior points by using the coordinate values from the boundaries. The resulting algebraic grid is not smooth in general because the slope discontinuities at the boundary propagate in the interior of the domain. That is why the mesh obtained by algebraic mapping is further improved by the use of Partial Differential Equations (PDE) technique in which a system of PDE is solved for obtaining the location of the grid points in the physical space. But in the computational space the transformed grid is of rectangular shape with uniform spacing. We can use any of the three types of partial differential equations, namely elliptic, parabolic and hyperbolic where elliptic equations are preferred for closed geometries, hyperbolic equations are used for domains with outer boundary not prescribed and similarly parabolic equations are used where boundary is closed on one side (prescribed) and open on the other. The present grid is generated using of elliptic partial differential equations. In any grid generation technique geometric information is fetched from the boundaries. Hence the steady state boundary valued nature of elliptic equations makes them most favorite and so they are widely used grid generation. A Laplace equation or a Poission equation with a Dirchlet boundary condition can be used for this purpose. Standard Poission equation is of the form

$$\nabla^2 \xi = P$$

$$\nabla^2 \eta = Q \tag{4.1}$$

Where P and Q are known as control functions.

If $P = Q = 0$ then, the equations get modified to Laplace form as

$$\nabla^2 \xi = 0$$

$$\nabla^2 \eta = 0 \tag{4.2}$$

The above equations can be solved by finite difference technique to get the location of the interior points from the boundary. The initial guess needed to solve the Laplace equation can be generated using algebraic mapping. This Laplacian operator can provide quite smooth grids. The grid lines remain equally spaced if boundary curvature is absent but near curved boundaries they show a tendency to concentrate. This drawback can be controlled with appropriate selection of control functions P and Q . Also control functions can be objectively employed for enforcing orthogonality over the selected edges. That may simplify implementation of boundary conditions, but use of control functions remains associated with additional complexity in the transformed domain.

4.2.2 Computational Procedure for Grid Generation

The algorithm used for the generation of the present grid can be outlined as follows:

1. Input is fed in the form of geometrical description.
2. The computational grid is defined on the curvilinear $\xi - \eta$ plane based on the number of grid points.
3. Boundary points along the edges of the physical domain are defined.
4. Now an initial guess is generated for the Laplacian by algebraic grid generation

method. This step uses just a linear interpolation scheme to compute the interior points.

5. The guess is improved a little by adopting simple four-point formula.
6. The actual Laplacian is in the form of

$$ax_{\xi\xi} - 2bx_{\xi\eta} + cx_{\eta\eta} = 0$$

$$ay_{\xi\xi} - 2by_{\xi\eta} + cy_{\eta\eta} = 0 \quad (4.3)$$

where

$$a = x_\eta^2 + y_\eta^2$$

$$b = x_\xi x_\eta + y_\xi y_\eta$$

is solved till convergence is obtained. Here subscripts indicate partial derivatives of Cartesian variables with respect to curvilinear variables.

The truncation error in numerical solutions is very much dependent on the nature of grid because it is here that the discretized approximation of differential equations is solved. We target for such a grid which gives minimum truncation error, and that requires testing of certain properties of the grid which have strong effect on the error. The parameters that affect these properties can be used to express the quality of the grid. These are

- Transformation Jacobian
- Skewness

- Aspect ratio
- Adjacent cell ratio

A desirable grid should have nonzero transformation jacobian almost at each location of the grid cells (they should be almost of similar order of magnitude with no quite small values appearing anywhere), least possible skewness, aspect ratio close to 6, and adjacent cell ratio close to one.

4.3 Finite Volume Method

The governing conservation equations are discretized using the finite volume approach of Eswaran and Prakash (1998). Here the solution domain is divided into a number of contiguous (finite) control volumes (CV) which are defined by the coordinates of their vertices assumed to be connected by straight lines. The coordinates of the control volume vertices are calculated by grid generation procedure. A collocated grid arrangement is employed and all the dependent variables (u, v, w, p, T) are defined at the same location - the centroid of the control volume (Figure 4.2). E, W, N, S, T and B indicate the six neighboring control volume centers for the east, west, north, south, top and bottom neighbors. The face center points e, w, n, s, t and b are located at the intersection of the lines joining the mid points of opposite edges. For example, te, be, ne, se are the midpoints of the edges that form the east face with e as the center of the cell face. The advantages of collocated grids over staggered grids have already been pointed out in Chapter-2 as explained by Peric et al. (1988). Before the time stepping can be done it is necessary to calculate geometrical parameters which include the surface vectors for the six faces e, w, n, s, t and b for each finite volume and its volume.

4.4 Surfaces and Volumes

The finite volume vertices are numbered 1 to 8 in the manner shown in Figure 4.2. The outward surface normals and volume can be found in the following manner as suggested by Kordulla and Vinokur (1983) and Eswaran et. al.(1995).

Defining $r_{ij} = r_i - r_j$ where r_i and r_j are the position vectors of points i and j respectively, we have expressions for surface area vectors of various faces given as follows

- East face

$$\vec{S}_e = \frac{1}{2}(\vec{r}_{74} \times \vec{r}_{83}) \quad (4.4)$$

- West face

$$\vec{S}_w = \frac{1}{2}(\vec{r}_{16} \times \vec{r}_{52}) \quad (4.5)$$

- North face

$$\vec{S}_n = \frac{1}{2}(\vec{r}_{27} \times \vec{r}_{63}) \quad (4.6)$$

- South face

$$\vec{S}_s = \frac{1}{2}(\vec{r}_{18} \times \vec{r}_{45}) \quad (4.7)$$

- Top face

$$\vec{S}_t = \frac{1}{2}(\vec{r}_{75} \times \vec{r}_{68}) \quad (4.8)$$

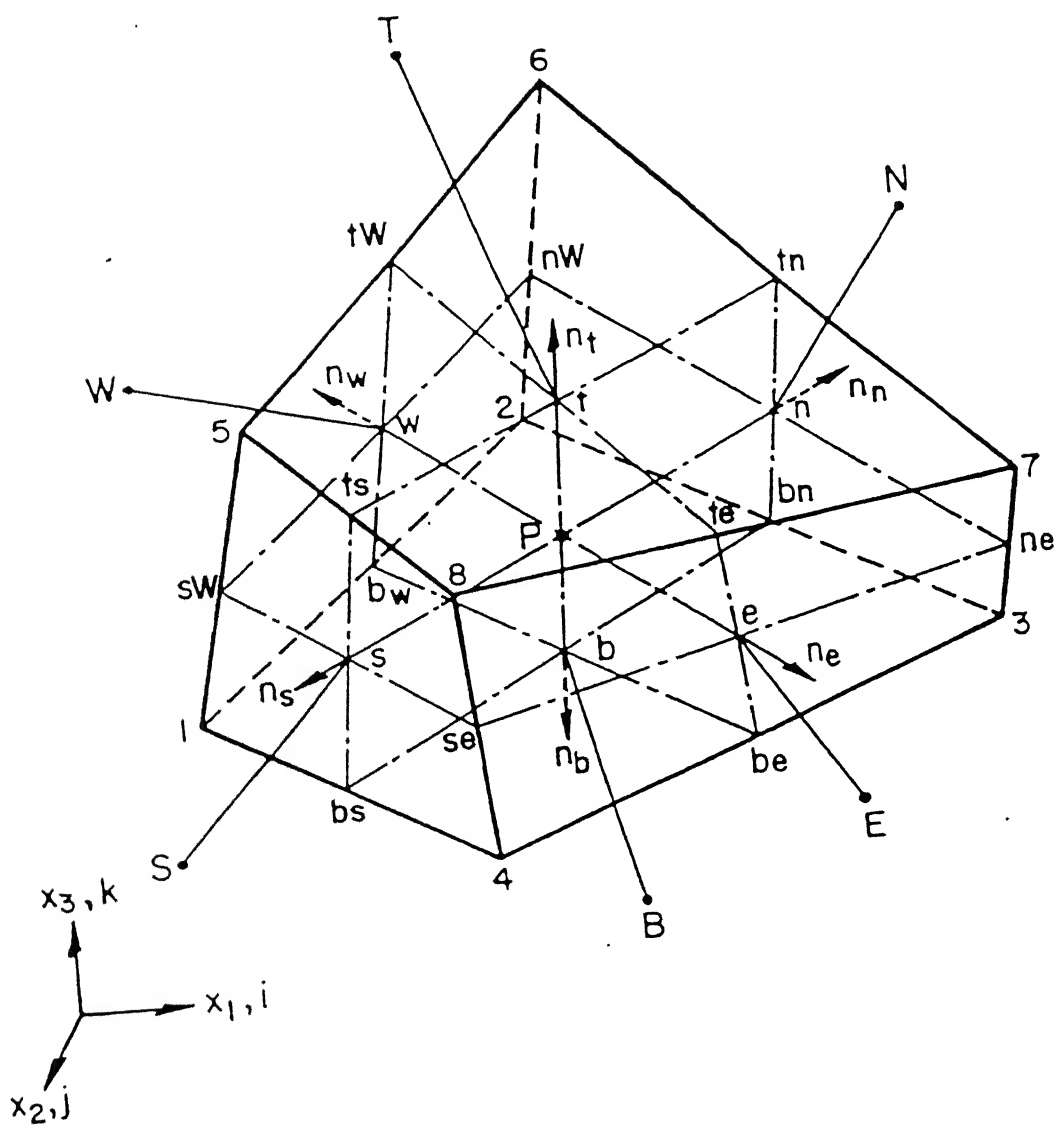


Figure 4.2 Three-dimensional finite volume cell

- Bottom face

$$\vec{S}_b = \frac{1}{2}(\vec{r}_{13} \times \vec{r}_{24}) \quad (4.9)$$

The volume of any cell is calculated using the cell coordinates, with the assumption that the linear segments to form the six cell faces join the cell corners (Eswaran and Prakash, 1998). The expression for volume of any cell becomes

$$V = \frac{1}{3} \vec{r}_{71} \cdot (\vec{S}_s + \vec{S}_b + \vec{S}_w) \quad (4.10)$$

4.5 Discretization Procedure

The main steps of the discretization procedure to calculate the convection and the diffusion fluxes and source terms are outlined below. The rates of change of integral fluxes and the source terms are integrated over the cell volume, whereas the convection and diffusion terms form the sum of fluxes through the faces of the control volume.

4.5.1 Discretization of Continuity Equation

Equation (3.1) is discretized in the following way:

$$\int_S \rho \vec{u} \cdot d\vec{S} \approx \sum_{j=e,w,n,s,t,b} \rho (\vec{u} \cdot \vec{S})_j = \sum \rho \vec{u}_j \cdot \vec{S}_j \quad (4.11)$$

where S_j is the surface vector representing the area of the j th cell face and u_j is the velocity defined at the face center j .

The discretized form of the continuity equation becomes

$$\sum_j F_j = F_e + F_w + F_n + F_s + F_t + F_b = 0 \quad (4.12)$$

where F_j is the outward mass flux through face j , defined by

$$F_j = \rho \vec{u}_j \cdot \vec{S}_j$$

4.5.2 Discretization of General Equation

(a) Rate of Change

The value of the dependent variable ϕ at the centroid of the control volume (the geometric center) represents an average over the CV as a whole. Thus

$$\frac{\partial}{\partial t} \int_V \rho \phi dV \approx \frac{(\rho \phi V)_P^{n+1} - (\rho \phi V)_P^n}{\Delta t} \approx \rho V \frac{\phi_P^{n+1} - \phi_P^n}{\Delta t} \quad (4.13)$$

where V is the volume of the cell.

(b) Convection Fluxes

The surface integral over convection flux of variable ϕ can be approximated in the following form

$$\int_S \rho \phi \vec{u} \cdot d\vec{S} \approx \sum_j \rho \phi_j (\vec{u} \cdot \vec{S})_j \approx \sum_j F_j \phi_j \quad (4.14)$$

where ϕ_j is the value of ϕ at the center of face j . Thus

$$\int_S \rho \phi \vec{u} \cdot d\vec{S} \approx F_e \phi_e + F_w \phi_w + F_n \phi_n + F_s \phi_s + F_t \phi_t + F_b \phi_b \quad (4.15)$$

where ϕ_e is the interpolated value of the variable ϕ at the east face center etc. This can be evaluated by using a central difference linear interpolation between the neighboring nodal

values ϕ_P and ϕ_E . At east face the value of ϕ_e is given by

$$\phi_e = \frac{V_E}{V_E + V_P} \phi_P + \frac{V_P}{V_E + V_P} \phi_E \quad (4.16)$$

where V_E and V_P are volumes of the cells around the points E and P respectively and ϕ_E and ϕ_P are the values of the dependent variables at these points. In a collocated grid system, all dependent variables are defined at the same location hence exactly the same interpolation scheme is used to express all of them at the interfaces. The central difference approximation to compute the convection flux may lead to numerical stability problems. Therefore the convection flux is blended with a first order upwind differencing scheme (UDS), and the difference between the central difference scheme (CDS) and UDS approximation as

$$F_e \phi_e = (F_e \phi_e)^{UDS} + \gamma \left[(F_e \phi_e)^{CDS} - (F_e \phi_e)^{UDS} \right] \quad (4.17)$$

The upwind differencing scheme is based on assumption that the convected cell face is equal to that at the upstream cell along the same coordinate direction. Thus the value ϕ_e at the east face is assigned the value ϕ_P if $u_e \geq 0$, i.e., the flux F_e is negative. This can be conveniently summarized as

$$\begin{aligned} F_e \phi_e &= \phi_P [[F_e, 0]] - \phi_E [[-F_e, 0]] \\ &+ \gamma \left\{ F_e \left(\frac{V_E}{V_E + V_P} \phi_P + \frac{V_P}{V_E + V_P} \phi_E \right) - \phi_P [[F_e, 0]] + \phi_E [[-F_e, 0]] \right\} \end{aligned} \quad (4.18)$$

The symbol $[[,]]$ signifies greater of the two quantities enclosed inside the brackets. Similar expressions can be written for the other cell faces (Eswaran et al. 1995).

$$F_w \phi_w = \phi_P [[F_w, 0]] - \phi_E [[-F_w, 0]]$$

$$+ \gamma \left\{ F_w \left(\frac{V_W}{V_W + V_P} \phi_P + \frac{V_P}{V_W + V_P} \phi_W \right) - \phi_P [[F_w, 0]] + \phi_E [[-F_w, 0]] \right\} \quad (4.19)$$

$$F_n \phi_n = \phi_P [[F_n, 0]] - \phi_N [[-F_n, 0]]$$

$$+ \gamma \left\{ F_n \left(\frac{V_N}{V_N + V_P} \phi_P + \frac{V_P}{V_N + V_P} \phi_N \right) - \phi_P [[F_n, 0]] + \phi_E [[-F_n, 0]] \right\} \quad (4.20)$$

$$F_s \phi_s = \phi_P [[F_s, 0]] - \phi_S [[-F_s, 0]]$$

$$+ \gamma \left\{ F_s \left(\frac{V_S}{V_S + V_P} \phi_P + \frac{V_P}{V_S + V_P} \phi_S \right) - \phi_P [[F_s, 0]] + \phi_S [[-F_s, 0]] \right\} \quad (4.21)$$

$$F_t \phi_t = \phi_P [[F_t, 0]] - \phi_T [[-F_t, 0]]$$

$$+ \gamma \left\{ F_t \left(\frac{V_T}{V_T + V_P} \phi_P + \frac{V_P}{V_T + V_P} \phi_T \right) - \phi_P [[F_t, 0]] + \phi_T [[-F_t, 0]] \right\} \quad (4.22)$$

$$F_b \phi_b = \phi_P [[F_b, 0]] - \phi_E [[-F_b, 0]]$$

$$+ \gamma \left\{ F_b \left(\frac{V_B}{V_B + V_P} \phi_P + \frac{V_P}{V_B + V_P} \phi_B \right) - \phi_P [[F_b, 0]] + \phi_B [[-F_b, 0]] \right\} \quad (4.23)$$

In a fully implicit method the upwind parts are implicit and they are incorporated in the coefficients of the unknown velocity during the pressure-velocity iteration. The CDS terms on the other hand are evaluated using the previous iteration values and used as a source term on the right side of the same equation. This is the so called deferred correction approach of Khosla and Rubin (1974). Multiplication of the explicit part of γ ($0 \leq \gamma \leq 1$) allows the introduction of numerical diffusion. For the first order upwind difference scheme $\gamma = 0$ and for the second order central difference $\gamma = 1$. The deferred correction approach enhances the diagonal dominance of the coefficient matrix. However, the present solution

scheme being explicit, the accuracy depends on the value of γ .

(c) Diffusion Fluxes

Peric (1985) developed the expression for the diffusion fluxes in the finite volume approach for first time. However, the exact expression in three dimensions are not explicitly available in open literature. Eswaran and Prakash (1998) evaluate the diffusion flux of a variable ϕ through the cell faces in the following manner

$$\int_S \Gamma_\phi \nabla \phi \cdot d\vec{S} \approx \sum_{j=e,w,n,s,t,b} \left(\Gamma_\phi \nabla \phi \cdot \vec{S} \right)_j = \sum_j -F_j^d \quad (4.24)$$

For any face we can write

$$\vec{S}_j = \alpha_1 \hat{n}^1 + \alpha_2 \hat{n}^2 + \alpha_3 \hat{n}^3 \quad (4.25)$$

where \hat{n}^1 , \hat{n}^2 and \hat{n}^3 are any three linearly independent (not necessarily orthogonal) unit vectors. Therefore

$$\nabla \phi \cdot \vec{S}_j = \nabla \phi \cdot (\alpha_1 \hat{n}^1 + \alpha_2 \hat{n}^2 + \alpha_3 \hat{n}^3) \quad (4.26)$$

$$= \alpha_1 \nabla \phi \cdot \hat{n}^1 + \alpha_2 \nabla \phi \cdot \hat{n}^2 + \alpha_3 \nabla \phi \cdot \hat{n}^3$$

If $\Delta\phi^1$, $\Delta\phi^2$, $\Delta\phi^3$ are the differences in ϕ between the two ends of the line segments ΔX^1 , ΔX^2 , ΔX^3 then

$$\Delta\phi^1 = \nabla \phi \cdot \Delta\vec{X}^1, \Delta\phi^2 = \nabla \phi \cdot \Delta\vec{X}^2, \Delta\phi^3 = \nabla \phi \cdot \Delta\vec{X}^3 \quad (4.27)$$

If $\Delta\vec{X}^1$, $\Delta\vec{X}^2$, $\Delta\vec{X}^3$ are in the directions \hat{n}^1 , \hat{n}^2 and \hat{n}^3 respectively then it follows from

Equation (4.27) that

$$\frac{\Delta\phi^1}{\Delta X^1} = \nabla\phi \cdot \hat{n}^1, \quad \frac{\Delta\phi^2}{\Delta X^2} = \nabla\phi \cdot \hat{n}^2, \quad \frac{\Delta\phi^3}{\Delta X^3} = \nabla\phi \cdot \hat{n}^3 \quad (4.28)$$

where ΔX^1 , ΔX^2 and ΔX^3 are the magnitudes of $\Delta\vec{X}^1$, $\Delta\vec{X}^2$ and $\Delta\vec{X}^3$. Combining Equations (4.26) and (4.28) we have

$$\nabla\phi \cdot \vec{S} = \alpha_1 \frac{\Delta\phi^1}{\Delta X^1} + \alpha_2 \frac{\Delta\phi^2}{\Delta X^2} + \alpha_3 \frac{\Delta\phi^3}{\Delta X^3} \quad (4.29)$$

To obtain α_1 , α_2 and α_3 we express

$$\hat{n}^1 = (n_{11}, n_{12}, n_{13})$$

$$\hat{n}^2 = (n_{21}, n_{22}, n_{23}) \quad (4.30)$$

$$\hat{n}^3 = (n_{31}, n_{32}, n_{33})$$

where n_{11} , n_{12} , n_{13} are the Cartesian components of \hat{n}^1 and which can be easily determined by $\frac{\Delta X_1^1}{\Delta X^1}$, $\frac{\Delta X_2^1}{\Delta X^1}$, $\frac{\Delta X_3^1}{\Delta X^1}$ where ΔX_1^1 , ΔX_2^1 , ΔX_3^1 are the three components of vector $\Delta\vec{X}^1$. The other values $n_{21} \dots n_{33}$ can be similarly obtained. Hence equation (4.22) can be written as a matrix equation involving n_{ij} (i, j = 1, 3) forming a known coefficient matrix of unknown column vector of α_1 , α_2 and α_3 related to Cartesian components of the surface vector \vec{S}_j as S_{1j} , S_{2j} , and S_{3j} .

Using Cramers rule in such a matrix equation we can solve for α_1 , α_2 and α_3 as follows

:

$$\alpha_1 = \frac{D_1}{D}, \alpha_2 = \frac{D_2}{D}, \alpha_3 = \frac{D_3}{D} \quad (4.31)$$

where D is the determinant of the coefficient matrix. D_1 is obtained by replacing the first column of D by the column with the elements S_{1j} , S_{2j} and S_{3j} .

The diffusion flux is made of two distinct parts - normal derivative diffusion flux and cross derivative diffusion flux. The second part arises from the non-orthogonality of the grid. The normal derivative diffusion flux is treated implicitly and is coupled with the implicit part of the convective flux to calculate the main coefficients of the discretized equations while the cross derivative diffusion flux is treated explicitly to avoid the possibility of producing negative coefficients in an implicit treatment. This term together with explicit part of convective flux is added to the source term. The example of east face is taken to illustrate the diffusion model (Figure 4.3). Given the edge center values ϕ_{te} , ϕ_{be} , ϕ_{se} , ϕ_{ne} we can get the normal diffusion term $\frac{\phi_E - \phi_P}{\Delta X^1}$, and the cross diffusion term $\frac{\phi_{te} - \phi_{be}}{\Delta X^2}$ and $\frac{\phi_{se} - \phi_{ne}}{\Delta X^3}$. Finally the diffusion flux is computed by

$$F_j^d = -\Gamma_\phi \left(\alpha_1 \frac{\phi_E - \phi_P}{\Delta X^1} + \alpha_2 \frac{\phi_{te} - \phi_{be}}{\Delta X^2} + \alpha_3 \frac{\phi_{ne} - \phi_{se}}{\Delta X^3} \right) \quad (4.32)$$

In order to find the edge center values for evaluation of cross derivative diffusion flux, the following interpolation scheme is proposed.

$$\phi_{te} = \frac{V_{TE}}{V_{tot}} \phi_P + \frac{V_P}{V_{tot}} \phi_{TE} + \frac{V_T}{V_{tot}} \phi_E + \frac{V_E}{V_{tot}} \phi_T \quad (4.33)$$

$$V_{tot} = V_{TE} + V_P + V_T + V_E$$

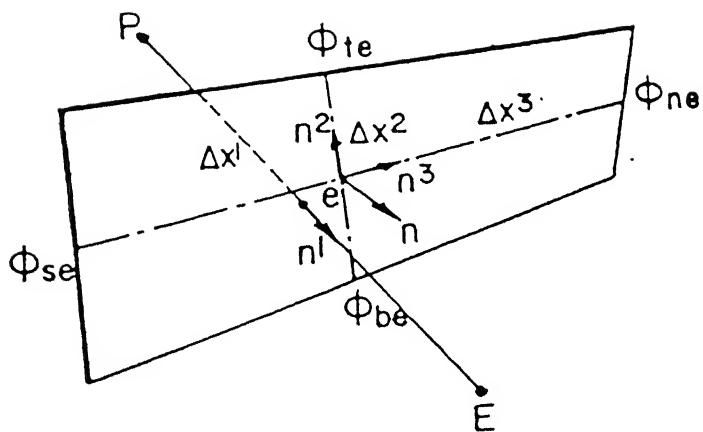


Figure 4.3 Face representation to illustrate diffusion model

$$\phi_{be} = \frac{V_{BE}}{V_{tot}}\phi_P + \frac{V_P}{V_{tot}}\phi_{BE} + \frac{V_T}{V_{tot}}\phi_E + \frac{V_E}{V_{tot}}\phi_B \quad (4.34)$$

$$V_{tot} = V_{BE} + V_P + V_B + V_E$$

$$\phi_{ne} = \frac{V_{NE}}{V_{tot}}\phi_P + \frac{V_P}{V_{tot}}\phi_{NE} + \frac{V_N}{V_{tot}}\phi_E + \frac{V_E}{V_{tot}}\phi_N \quad (4.35)$$

$$V_{tot} = V_{NE} + V_P + V_N + V_E$$

$$\phi_{se} = \frac{V_{SE}}{V_{tot}}\phi_P + \frac{V_P}{V_{tot}}\phi_{SE} + \frac{V_S}{V_{tot}}\phi_E + \frac{V_E}{V_{tot}}\phi_S \quad (4.36)$$

$$V_{tot} = V_{SE} + V_P + V_S + V_E$$

where V_{TE} is the volume of the cell that is located at the top east of the cell P. The other edge center values of the dependent variables can be interpolated in a similar way.

(d) Sources

The source term is to be integrated over the cell volume. The contribution of a source term in the discretized equation may be thought of

$$\int_v S_\phi dV \approx (S_\phi)_P V \quad (4.37)$$

Apart from the real source S_ϕ , explicitly treated parts of the convection and diffusion fluxes maybe added to S_ϕ . The momentum equations contain pressure terms. These terms are also treated explicitly. Its discretization is analogous to that of the ordinary diffusion flux, i.e., for the i th momentum equation the pressure term is

$$-\int_S p \hat{n}_i \cdot d\vec{S} \approx \sum_j p_j S_{ij} \quad (4.38)$$

where p_j is the pressure at the j th face center and S_{ij} is the i th component of the source vector for face j .

4.6 Pressure and Velocity Coupling

The velocity and pressure field satisfying the mass and momentum conservation laws can be found using a procedure akin to Simplified Marker and Cell (SMAC) method. This method offers an efficient and easy way of pressure velocity coupling. It is basically a semi explicit method. The momentum equations are discretized in an explicit manner with the exception of the pressure gradient terms that are treated implicitly, and the continuity equations are also enforced implicitly. This can be expressed mathematically by the following two discretized equations of momentum and continuity

$$\rho V \frac{u_P^{n+1} - u_P^n}{\Delta t} + \sum_j (F^c + F^d)^n = - \sum_j p_j^{n+1} S_{ij} \quad (4.39)$$

and

$$\sum_j F_j^{n+1} = 0 \quad (4.40)$$

The momentum equations are solved using the guess values of velocity and pressure field. The provisional velocity components u_i^* are calculated from the following equation

$$u_P^* = u_P^o - \frac{\Delta t}{\rho V_P} (F_P^c + F_P^d) + \frac{\Delta t}{\rho V_P} S_u \quad (4.41)$$

where u_P^o is the value of velocity at earlier iteration and S_u is the pressure term. This provisional velocity in general will not satisfy the continuity equation. The continuity Equation (4.40) in another form reads as follows:

$$\sum_j (F_j^* + F_j') = 0$$

$$\sum_j F_j' = - \sum_j F_j^* \quad (4.42)$$

where F_j^* is the uncorrected mass flux obtained from the provisional velocities and F_j' is the mass flux correction. To evaluate the terms on the right side of the Equation (4.42) it is necessary that the variables (velocities and pressure) are to be known at the cell faces. Due to the non-staggered arrangement if the variables at the cell faces are evaluated by linear interpolation between the adjacent cell center quantities then the pressure iteration does not converge. The solution leads to a Checker Board pressure field (i.e., spurious oscillation of pressure may occur) as shown by Rhie (1981). This problem can be circumvented by using the concept of Momentum Interpolation (Majumdar, 1988). The essence of the concept is that the velocities at the cell faces are computed by linear interpolation of

the convective and diffusive terms but not the pressure term. Thus the method with the collocated variable arrangement relies indirectly on the staggering idea. Following this idea the interpolated velocity at the east face of the control volume is obtained in the following manner

$$u_e = \overline{(v_P, v_E)} - \frac{\Delta t}{\rho} \nabla p \quad (4.43)$$

where

$$v_P = u_P^\circ - \frac{\Delta t}{\rho V_P} (F_P^c + F_P^d) \quad (4.44)$$

$$v_E = u_E^\circ - \frac{\Delta t}{\rho V_E} (F_E^c + F_E^d) \quad (4.45)$$

and the over bar indicates a linear interpolation using equation (4.16). So the uncorrected mass flux for the east face using Equation (4.43) becomes

$$F_e^* = \rho \vec{u}_e \cdot \vec{S}_e = \rho \overline{(\vec{v}_P, \vec{v}_E)} \cdot \vec{S}_e - \Delta t \nabla p \cdot \vec{S}_e \quad (4.46)$$

Equation (4.46) in its generalized form for any cell face is in the for

$$F_j^* = \rho \vec{v}_j \cdot \vec{S}_j - \Delta t \nabla p_j \cdot \vec{S}_j \quad (4.47)$$

To enforce mass conservation, the velocity and pressure corrections are introduced, linked by

$$u'_j = \frac{\Delta t}{\rho} \nabla p'_j \quad (4.48)$$

This step simulates the effect of a staggered grid (face-center velocity and cell-center pressure) and reaps the benefits of faster convergence. From Equation (4.48) we get the mass flux correction at the face j

$$F'_j = \rho u'_j \cdot S_j = -\Delta t \nabla p'_j \cdot S_j \quad (4.49)$$

Since Equation (4.49) is exactly of the same form as equation for diffusion flux Equation (4.24), with only the variable interchanged, therefore the same method can be used for computing F'_j . Combining Equations (4.42) (4.47), and (4.49) yields

$$-\Delta t \nabla p'_j \cdot \vec{S}_j = \rho \vec{V}_j \cdot \vec{S}_j - \Delta t \nabla p_j \cdot \vec{S}_j$$

or

$$\Delta t \nabla p'_j \cdot \vec{S}_j + S_m = 0 \quad (4.50)$$

$$(S_m = \rho \vec{V}_j \cdot \vec{S}_j - \Delta t \nabla p_j \cdot \vec{S}_j)$$

which gives the pressure correction. After the solution of the pressure correction equation, the nodal velocity, mass fluxes and pressure are updated. The corrected pressure p^{n+1} is obtained by

$$p^{n+1} = p^n + p' \quad (4.51)$$

Instead of solving Equation (4.39) again with the corrected pressure field, velocity calcu-

lations can be corrected in the fore

$$\vec{u}'_P = -\frac{\Delta t}{\rho V_P} \sum_j p'_j \vec{S}_j \quad (4.52)$$

The corrected velocity field u_i^{n+1} is obtained by

$$u_i^{n+1} = u_i^* + u'_i \quad (4.53)$$

Using this new velocity distribution, the energy equation is discretized and solved. On integrating the conservative form of the steady state energy equation over a control volume (neglecting the dissipative terms as it is significant for high speed flows), we arrive at the following temperature equation

$$\alpha \sum_j \left(\nabla T \cdot \vec{S} \right)_j = \sum_j \left(\rho \vec{u}_j \cdot \vec{S}_j \right) T_j \quad (4.54)$$

which is solved iteratively to get the temperature distribution of the current time step.

The first terms of Equation (4.50) and Equation (4.54) are expanded following the philosophy that was followed during the discretization of Equation (4.24). Subsequent regrouping of the normal derivative terms yields the standard *Poisson Equation*. The Poisson equation can be solved by a multitude of methods. We have used Gauss Seidel iteration method. This method is quite reliable and robust. The flow chart with the main steps of the algorithm is given in Figure 4.4.

4.7 Solution Algorithm

The velocity, pressure and temperature are calculated by the following procedure of Eswaran and Prakash (1998). The procedure can be summarized in the following way:

1. Make initial guess of the pressure, velocity and temperature fields. Use Equations

(4.41) and (4.44) to calculate cell center velocities u_P and v_P . use linear interpolation {Equation(4.16)} to obtain the face center quantities v_j .

2. Compute the mass flux through cell face j using equation (4.47) i.e.,

$$F_j^* = \rho \vec{v}_j \cdot \vec{S}_j - \Delta t \nabla p_j \cdot \vec{S}_j$$

3. Use equation (4.48) to compute the flux correction at the cell face j using Equation (4.49) i.e.,

$$F_j' = -\Delta t \nabla p_j' \cdot \vec{S}_j$$

This is computed using the formulation for diffusion fluxes [Equations (4.24) - (4.36)].

For calculating F_j' , the variable ϕ is to be replaced by p' .

4. Compute the residue, \Re for each cell,

$$\Re = -\sum F_j^* - \sum F_j'$$

5. Calculate the cell-center pressure correction (using Gauss-Seidel method) from the relation

$$p_p' = p_p' + \omega \frac{\Re}{a_p \Delta t}$$

where ω is the relaxation factor and a_p stands for the diagonal coefficients of Equation (4.50), which is calculated from

$$a_p = -\left[\frac{\alpha_1}{\Delta X^1} \Big|_w - \frac{\alpha_1}{\Delta X^1} \Big|_e + \frac{\alpha_2}{\Delta X^2} \Big|_n - \frac{\alpha_2}{\Delta X^2} \Big|_s + \frac{\alpha_3}{\Delta X^3} \Big|_b - \frac{\alpha_3}{\Delta X^3} \Big|_t \right]$$

where α_1, α_2 etc. are the same as that are used in Equations (4.24 - 4.36).

6. If $\Re_{rms} > \epsilon$ go to step 3.

7. Store the updated mass flux through the cell faces using Equation (4.47)

$$F_j^* = \rho \vec{v}_j \cdot \vec{S}_j - \Delta t \nabla p_j \cdot \vec{S}_j$$

8. Store the updated pressure at the center of the cells

$$p_P = p_P + p'_P$$

9. Store the cell center corrected velocity

$$u'_P = -\frac{\Delta t}{\rho V_P} \sum_j p'_j S_{ij}$$

$$u_P = u_P + u'_P$$

10. Calculate the residual for each cell

$$\tilde{\Re} = \sum_j \rho \left(\vec{u}_j \cdot \vec{S}_j \right) T_j - \alpha \sum_j \left(\nabla T \cdot \vec{S} \right)_j$$

11. Calculate the cell center temperature using Gauss-Seidel method, to obtain

$$T_P = T_P + \Omega \frac{\tilde{\Re}}{b_P \alpha}$$

where Ω is the relaxation factor and b_P stands for the diagonal coefficients of Equa-

tion (4.54) i.e., calculated from the relation

$$b_P = -a_P$$

12. If $\tilde{\mathfrak{R}}_{rms} > \epsilon$ go to 10.

13. Go to step 1 and repeat the process until the steady state is reached. It can be shown that solving Equation (4.42) is same as solving

$$\nabla^2 p' = -\rho \frac{\nabla u_i^*}{\Delta t}$$

and finding the corrections

$$u'_i = -\frac{\Delta t}{\rho} \nabla p'$$

such that

$$u_i^{n+1} = u_i^* + u'_i$$

$$p^{n+1} = p^n + p'$$

Thus the procedure above can be called solution of *Pressure Linked Equations*.

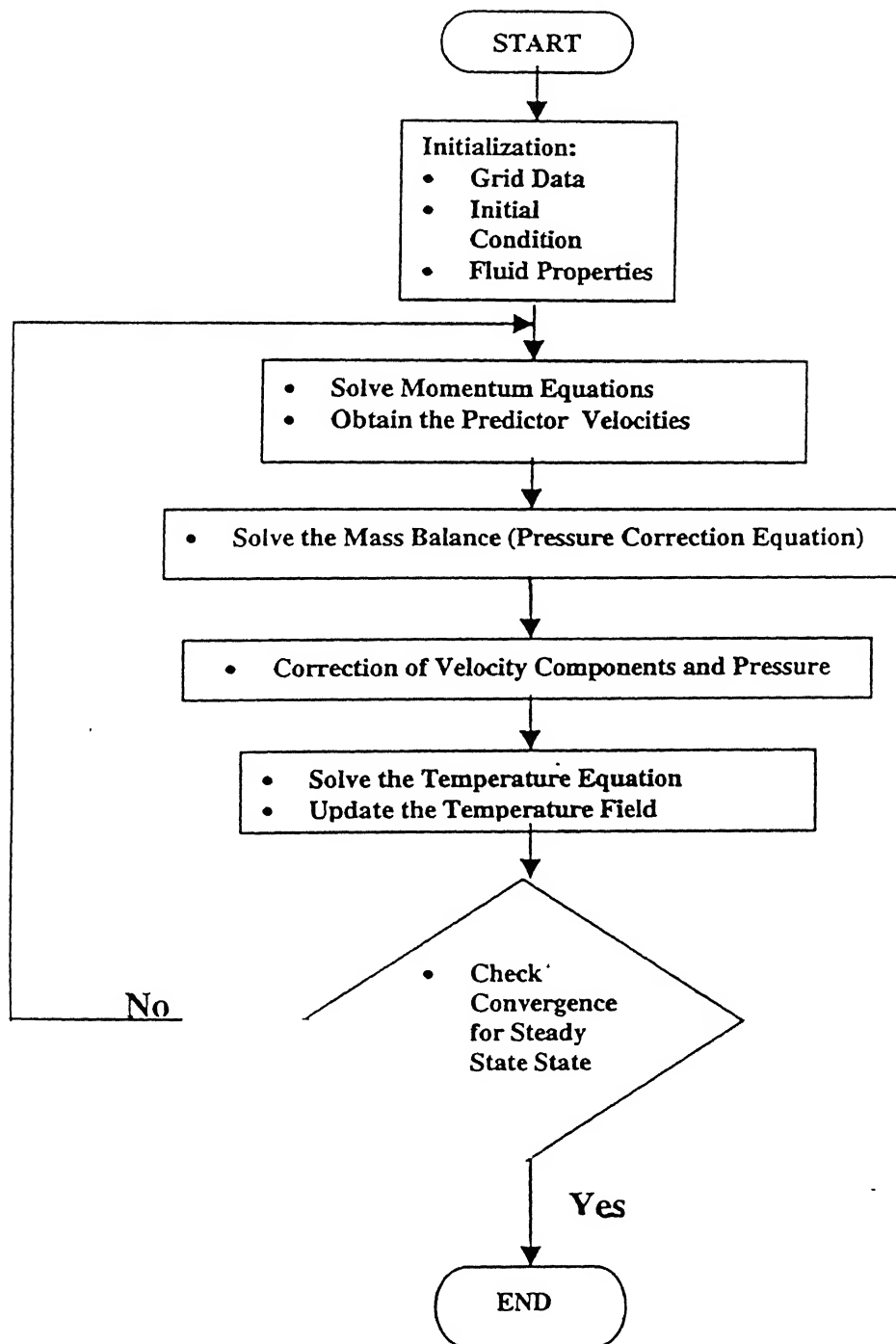


Figure 4.4 Iterative Solution Scheme

4.8 Numerical Stability Considerations

The Semi-Explicit method used here relies on explicit differences and suffers from time step restrictions. For a given mesh the choice of the time step is determined through stability analysis which has to take care of two conditions. First, fluid should not be allowed to cross more than one cell in any one time step. This restriction is derived from the Courant-Friedrich-Lewy (CFL) criterion of stability given by

$$\delta t_1 < \min \left\{ \frac{\delta x}{|u|}, \frac{\delta y}{|v|}, \frac{\delta z}{|w|} \right\} \quad (4.55)$$

where the minimum is with respect to every cell in the domain. Typically δt is chosen equal to one-third to two-third of the minimum cell transient time.

Secondly, when a nonzero value of kinematic viscosity is used, momentum must not diffuse more than one cell in one time step. A linear stability analysis shows that the restrictions on grid Fourier number in this case will yield

$$\delta t_2 < \frac{1}{2} \frac{(\delta x)^2 (\delta y)^2 (\delta z)^2}{(\delta x)^2 + (\delta y)^2 + (\delta z)^2} Re \quad (4.56)$$

Finally the minimum of the above two time increments is chosen for computation.

5 RESULTS AND DISCUSSION

5.1 Introduction

A three-dimensional numerical solution of flow and heat transfer for a plane channel with built-in circular tube and delta winglets in *common flow down* arrangement is presented in this section. A $51 \times 41 \times 17$ grid-mesh is used and the computations have been carried out for Reynolds number of 500, 1000 and 1410 and at different angles of attack. The divergence free criterion is satisfied using an upper bound of 10^{-4} . The blockage ratio (D/B) is fixed at 0.25. Air has been taken as the working fluid, hence the Prandtl number of the present study is 0.7. The heat transfer characteristics have been compared on the basis of spanwise averaged Nusselt number ($\overline{Nu_s}$) based on bulk mean temperature(T_b). The entire analysis in this section is based on the time-averaged flow and temperature fields.

5.2 Flow and Heat Transfer Characteristics in a Rectangular Channel with built-in Circular Tube

In this section detailed analysis of flow and heat transfer characteristics for rectangular channel with a built-in circular tube is presented. The results presented here are for a Reynolds number of 1000.

5.2.1 Flow Characteristics

Figure 5.1 shows the streamline plot on the horizontal mid plane of the channel i.e. at $z = H/2$. The figure clearly shows the two symmetrical standing vortices at location A. These are the von Karman vortices. The flow separation in the wake region of the tube is clearly established.

The limiting streamline plot in the region close to the plate is shown in Figure 5.2. A

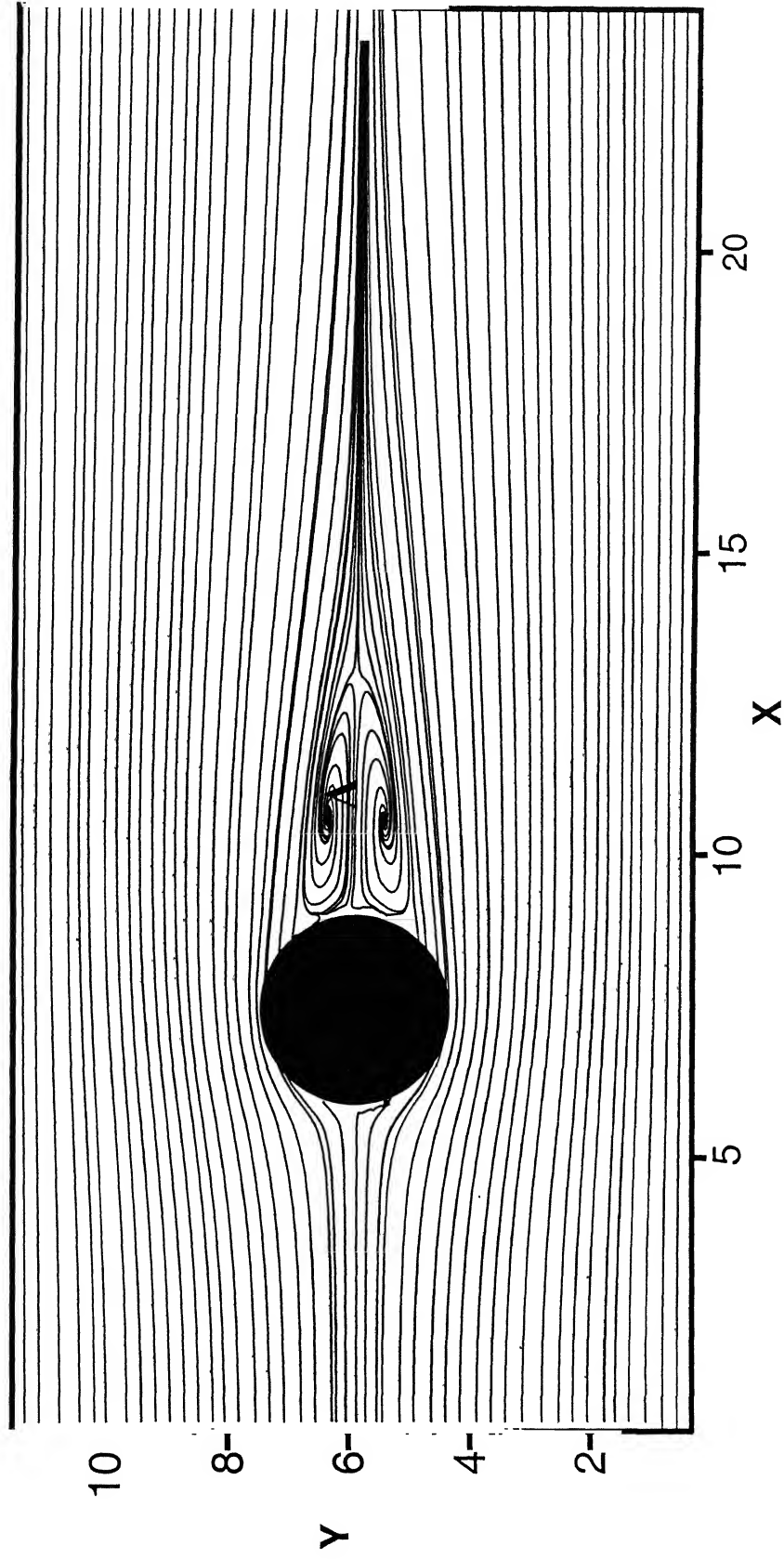


Figure 5.1 Streamline plot on horizontal midplane

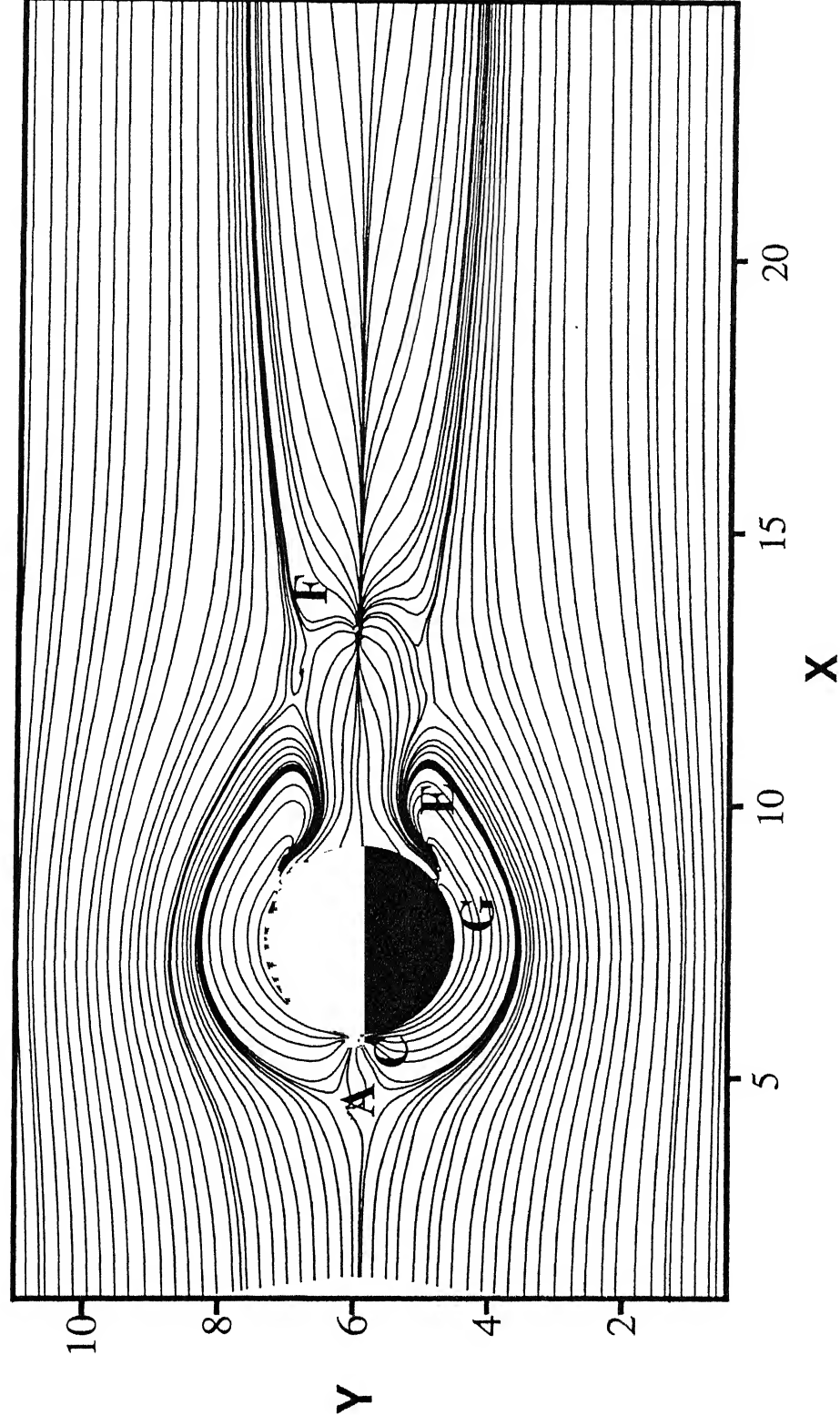


Figure 5.2: Limiting Streamlines on a plane close to the bottom plate

saddle point of separation and a horseshoe vortex system is observed from the figure. The incoming flow does not separate in the traditional sense but reaches a stagnation or saddle point of separation (marked A) and goes around the body. The nodal point of attachment (marked C) and the separation lines which form circular arcs across the tube are seen in the figure. The flow above the lower wall hits the front of the tube. A significant part of it moves downward and creates a region of reversed flow in front of the stagnation line. On each side of the tube, one finds a region of converging streamlines (marked G). These are the traces of horse shoe vortices. Behind the body one finds two areas of swirling flow (marked E) which are the footprints of an arch vortex. There is a wake stagnation point (marked F) further downstream of the body.

Figure 5.3 shows streamline plot on the vertical midplane. The wake of the cylinder exhibits a strong three-dimensional behavior. The strong normal velocity component, w is caused by pressure gradient in the vertical direction in the wake region. The figure clearly shows the footprints of the horseshoe vortices (marked as S_1 and S_2) and the reattachment line or the wake stagnation line (marked S_3).

The horseshoe vortices (S_1 and S_2) are initiated near the junction of cylinder and the channel walls. The formation of these vortices is displayed in Figure 5.4. As the fluid approaches the stagnation line of the cylinder, its velocity head contributes to total pressure. The velocity in the boundary layer on the channel walls increases in the vertical direction away from walls. This results in stagnation pressure gradient. This causes flow towards the walls which interacts with the main stream. The fluid rolls up forming vortices which are swept around the cylinder base and are carried down stream. This results in formation of horseshoe vortices which form a pair of counter rotating longitudinal vortices.

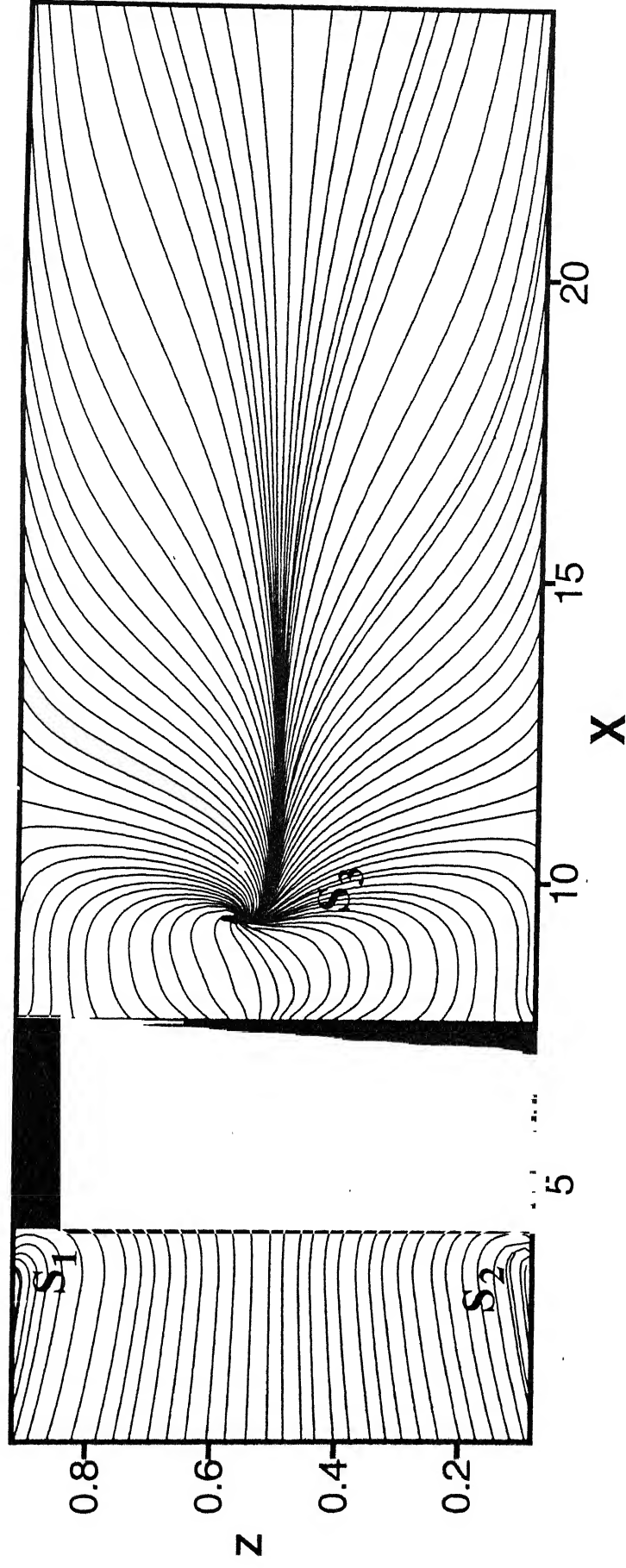


Figure 5.3: Streamline plot on vertical mid-plane

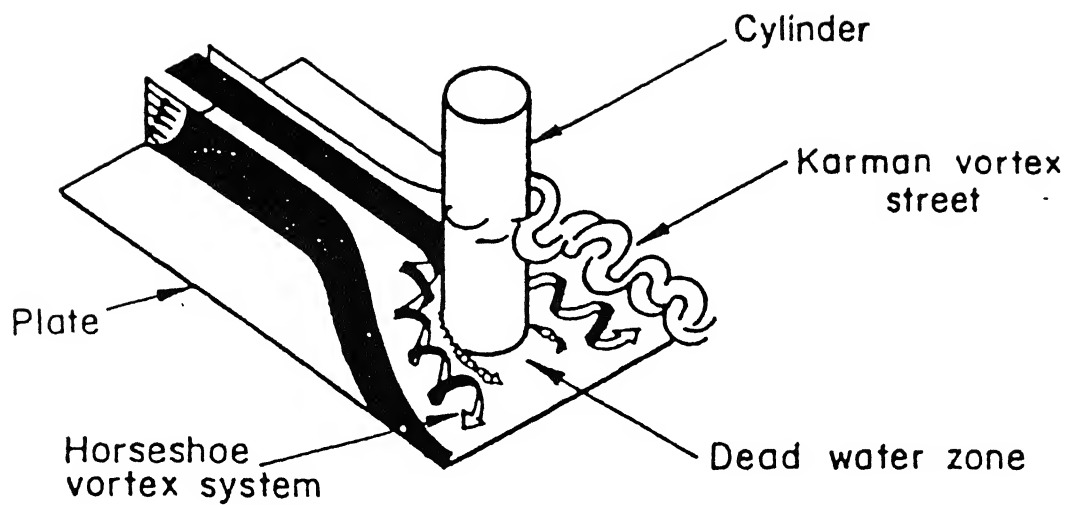


Figure 5.4 Flow around a cylinder on a flat plate

पुस्तकालय काशीनाथ केलकर पुस्तकालय
 भारतीय प्रायोगिकी संस्थान कानपुर
141869
 अवाप्ति क्र. A

5.2.2 Heat Transfer Characteristics

Figure 5.5 shows the distribution of spanwise average Nusselt number based on bulk mean temperature ($\overline{Nu_s}$) for rectangular channel and rectangular channel with built-in circular tube. The $\overline{Nu_s}$ at the leading edge, for both cases, is very high due to large temperature difference between the incoming colder fluid and the hot channel walls. In rectangular channel $\overline{Nu_s}$ decreases continuously in downstream direction. The velocity boundary layer is predominantly two-dimensional, and the cross flow is negligible. Hence, same fluid particles are in contact with the channel walls. As a result, the temperature difference between the fluid and channel walls decreases and hence $\overline{Nu_s}$ decreases in flow direction.

Figure 5.6 shows iso-Nusselt number plot on the bottom plate for plane channel with built-in circular tube. Figures 5.5 and 5.6 show an abrupt increase of Nusselt number at the location of circular tube. This is due to formation of horseshoe vortex system that consists of two counter-rotating longitudinal vortices as already shown in Figure 5.4. These vortices interact with predominantly two-dimensional boundary layer and produce a three-dimensional swirling flow that mixes the near wall fluid with the free stream. This leads to disruption of thermal boundary layer causing enhancement of heat transfer and increase in span averaged Nusselt number. The wake zone behind the tube is a separated dead water zone. It has fluid recirculating at very low velocity and so heat transfer in this zone is quite poor.

5.3 Flow Field in Plane Channel with a Built-in Circular Tube and Winglet Pair

This section presents a detailed analysis of flow in a rectangular channel with a built-in circular tube and winglet pair. The results correspond to a Reynolds number of 1000. Figure 5.7 shows the streamline plot of the flow field on the horizontal midplane of the

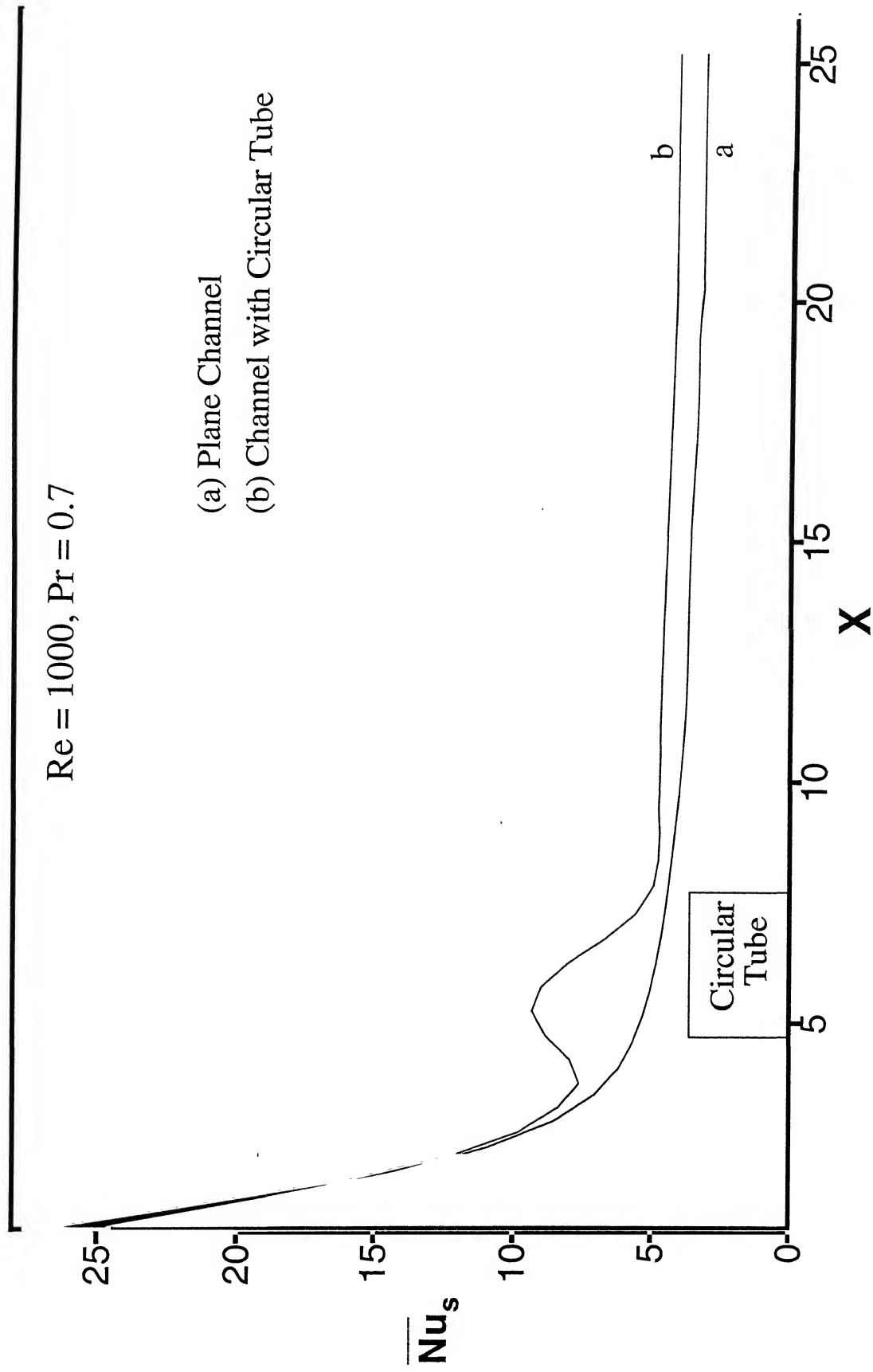


Figure 5.5: \overline{Nu}_s for Plane Channel and Channel with Circular Tube

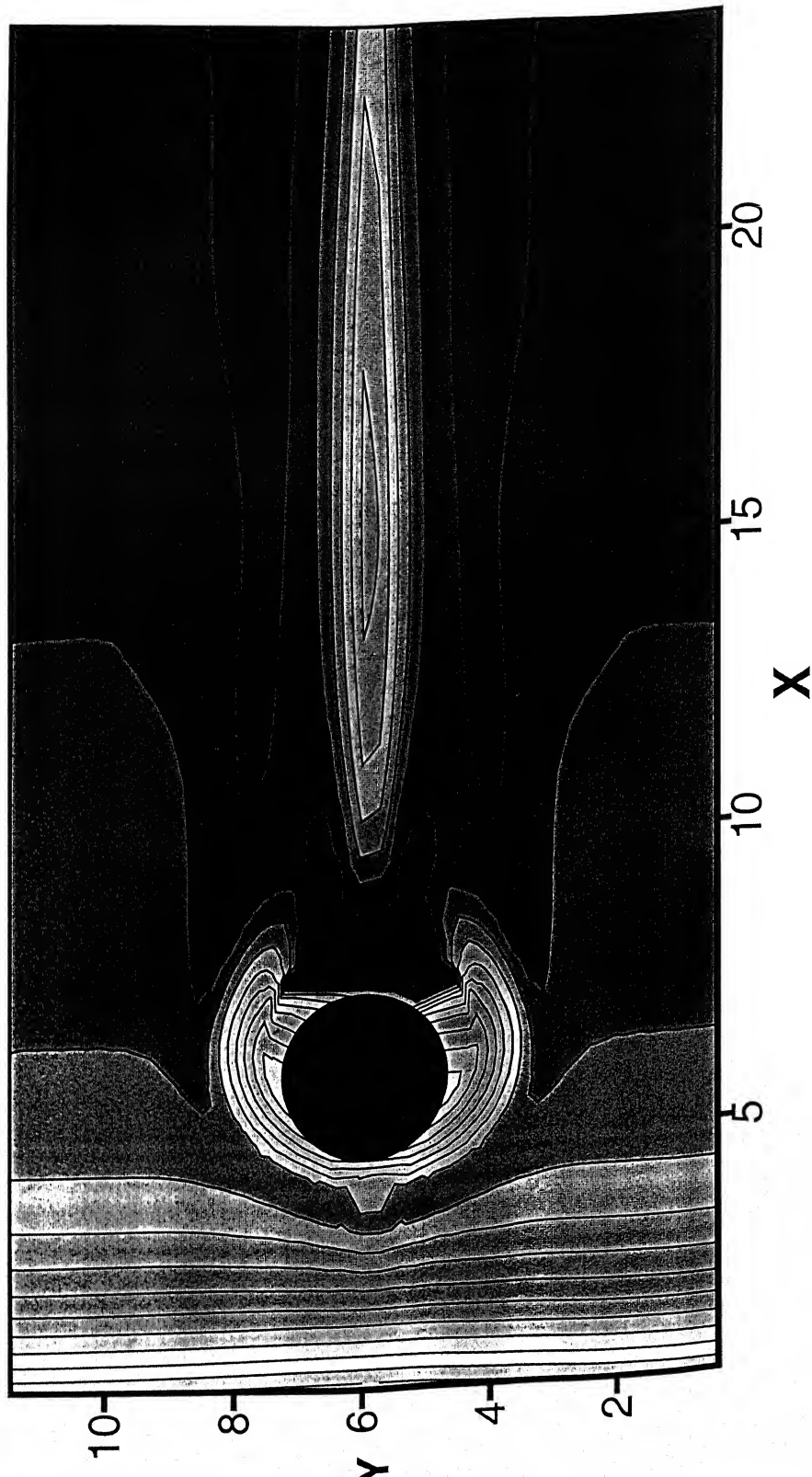
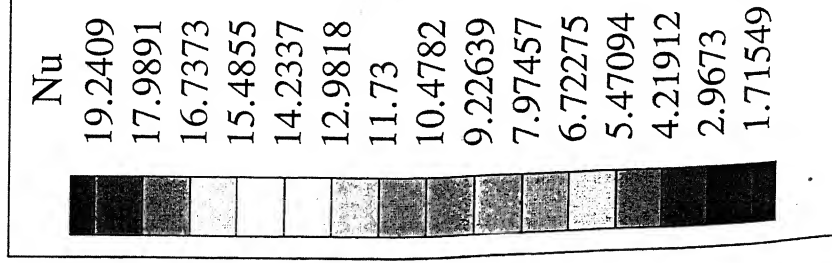


Figure 5.6: Iso-Nusselt number plot on the bottom plate

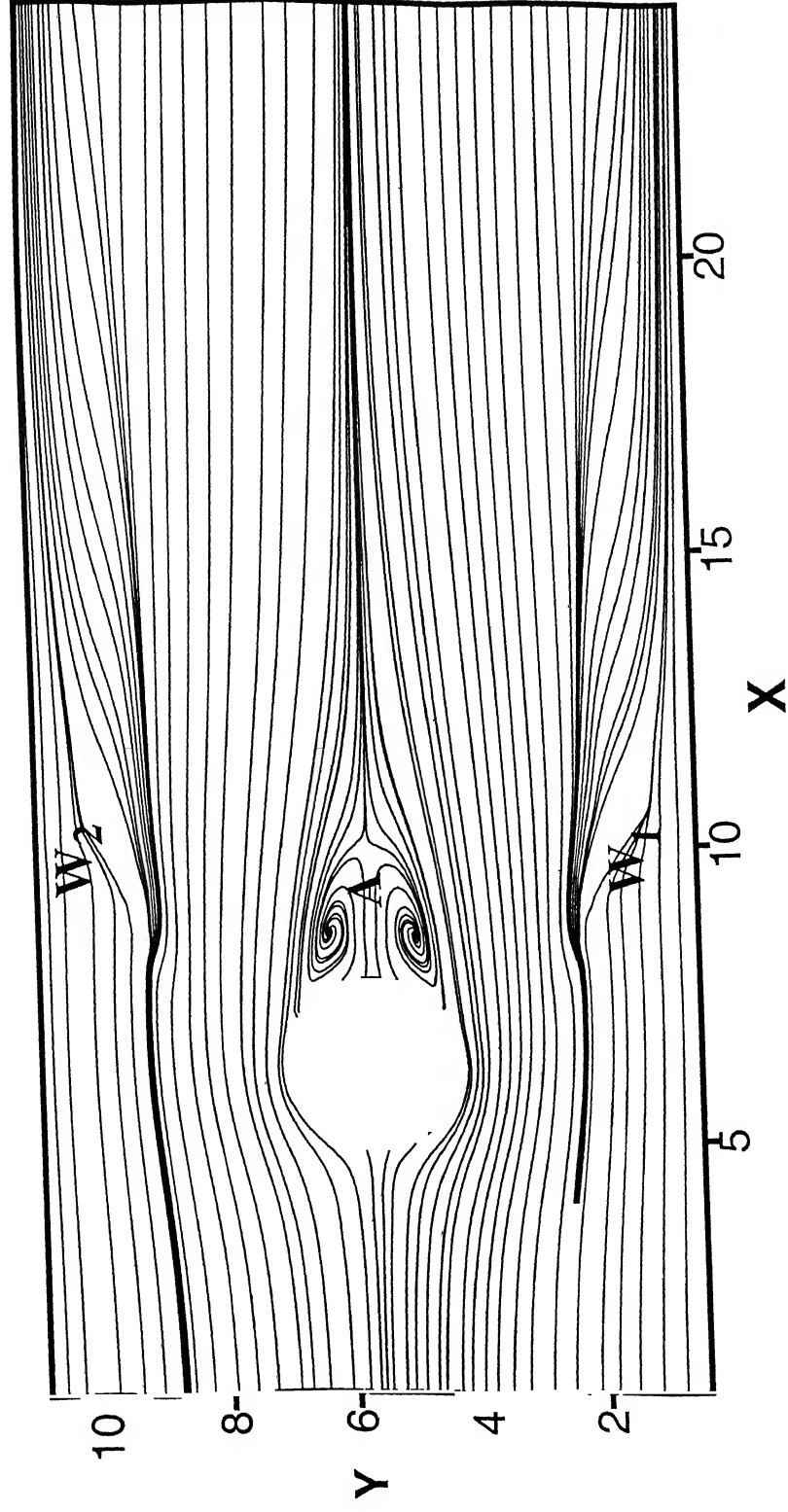


Figure 5.7: Streamlines on the horizontal mid-plane of the channel

channel at $z = H/2$. The flow separation and the wake formation are clearly visible. The wake is symmetric at this stage. Point A shows the saddle point of separation and W_1, W_2 show the location of winglets. Figure 5.8 shows the limiting streamlines for the velocity field on a horizontal plane close to the bottom wall for the Reynolds number of 1000. The winglet pair brings about a swirling motion, which has a dominant component of transverse motion. The transverse momentum transfer to otherwise separated boundary layer delays the separation. A saddle point of separation and a horseshoe vortex system are observed in the figure. The incoming flow reaches a stagnation point or a saddle point of separation (marked A) and goes around the body. The nodal point of attachment (marked C) and separation lines are also visible. On each side of the tube, one finds a region of converging streamlines (marked G). These are the traces of the horseshoe vortices. Behind the tube one finds two zones of swirling flow (marked E) which are foot prints of an arch vortex. The wake stagnation point F is located at a distance slightly more than one diameter in the downstream. The winglets are located at W_1 and W_2 . The twisted streamlines, indicating the swirling motion are visible around the winglets.

5.3.1 Vortex Formation by Delta Winglets

Figure 5.9 shows the vortices generated by the winglet. It generates two types of vortices, namely, main vortices and horseshoe vortices. Horseshoe vortices are induced due to velocity variation in boundary layer over the base plate. The mechanism is similar to the formation of the horseshoe vortex system generated in flow past a circular tube as explained in section 5.2.1. Main vortices are created due to pressure difference between the pressure side and the suction side of the winglets.

Figure 5.10 (a) , (b), (c) show cross-stream velocity vectors at various axial locations in the channel with the circular tube and the winglet pair as the built-in obstacles. Schematic location of the winglet pair is shown in Figure 3.1. The view-window of this figure is near

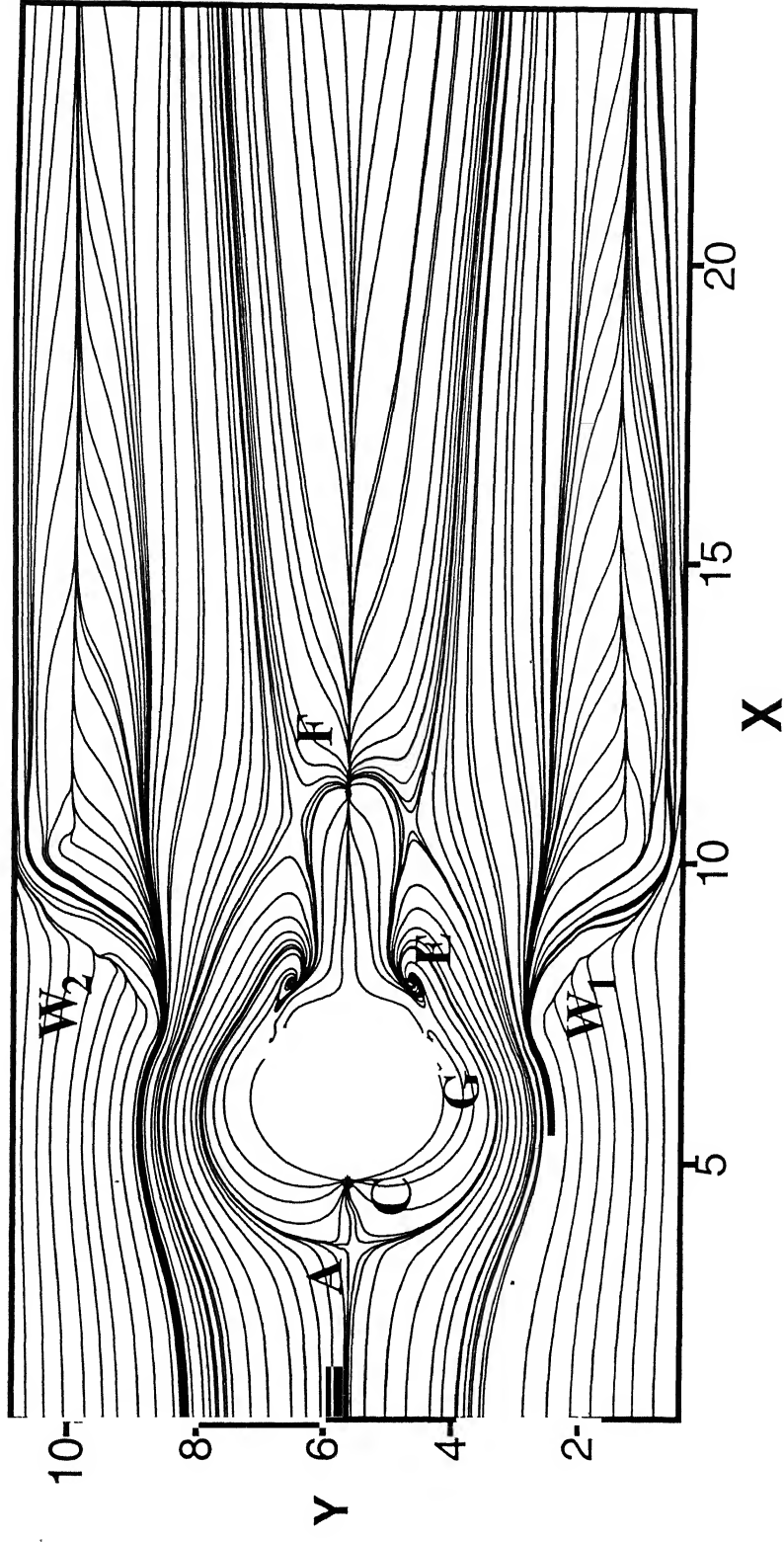


Figure 5.8: Limiting streamlines on a plane close to the bottom plate

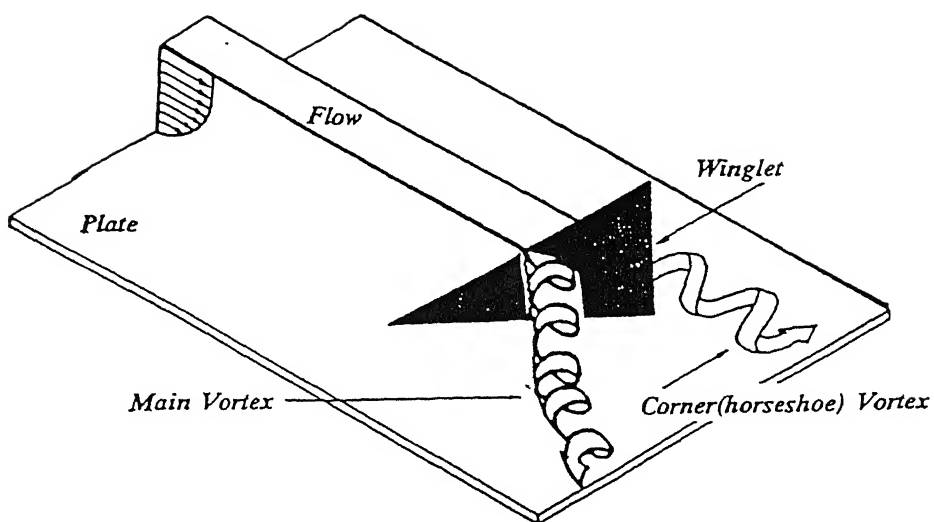


Figure 5.9 The wake structure generated by a winglet

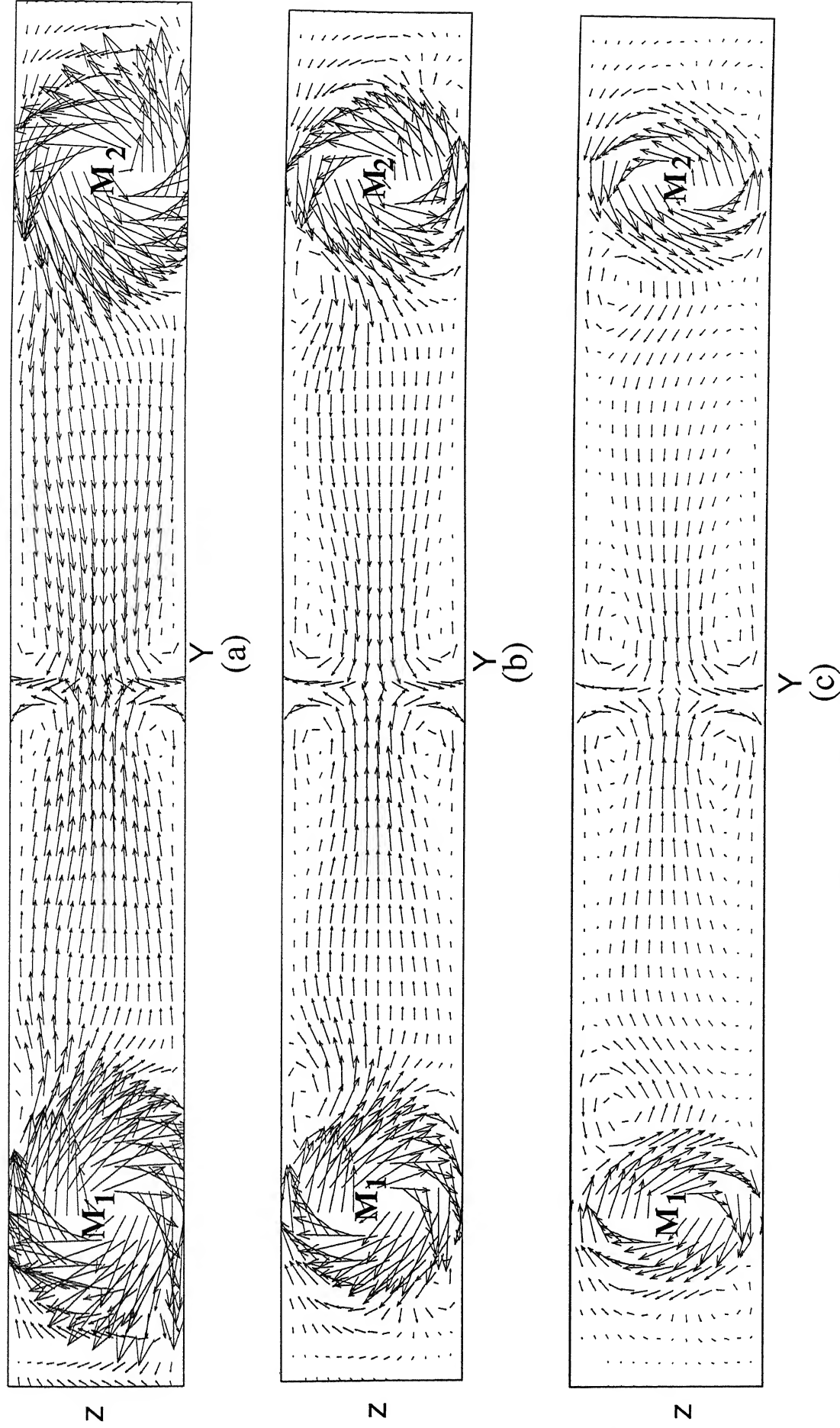


Figure 5.10 Streamline plot in cross plane at various X locations
(a) $X = 11$, (b) $X = 16$, (c) $X = 21$

the exit plane. The axial location of Figure 5.10(a) is at the immediate downstream of the trailing edge of the winglet pair. The velocity vectors depict the secondary flow pattern on various cross-stream planes in the channel. The results correspond to a Reynolds number of 1000 and $\beta = 30^\circ$. The pressure difference between pressure surface and suction surface of the winglet induces a complex vortex system. The vortex system generally behaves like a free vortex motion (apparent from the velocity vectors), with the exception of the core region where a rotational (forced) vortex motion persists. The vortices are also longitudinal vortices, since the axes of the vortices are parallel to the main flow direction. The longitudinal vortices are centered at M_1 and M_2 . The swirl, imposed by the longitudinal vortices, serves in creation of downwash on the bottom plate. The figure clearly reveals that the secondary flow on the cross stream planes describes a *common-flow-down* situation. Mendez et al. (1998) have explained the kinematics of flow and mechanism of transport enhancement due to the longitudinal vortices. The strength of the vortex motion decreases in the downstream due to viscous resistance initiated at the confining walls. Vortex interaction with common flow between the vortices directed towards the wall has been extensively studied by Pauley and Eaton(1998). The downwash causes strongest distortion of the boundary layer over the greatest streamwise distance. Figure 5.11 displays the basic flow structure for the swirling nature of the flow in both *common-flow-up* and *common-flow-down* configurations. The resulting downwash fountain in *common-flow-down* configuration may be observed in the figure for our case of counter-rotating vortex pair.

Figures 5.12 (a), (b) and (c) represent the streamlines on the cross stream plane at different axial locations, namely at $X=11$, $X=16$ and $X=21$ in the channel. Here M_1 and M_2 are the main vortices generated by the winglets. Also are shown the horseshoe vortices H_1 and H_2 generated by winglets. These vortices are also called corner vortices (Biswas et al. (1996)). The streamlines confirm the existence of a strong vortical motion. The

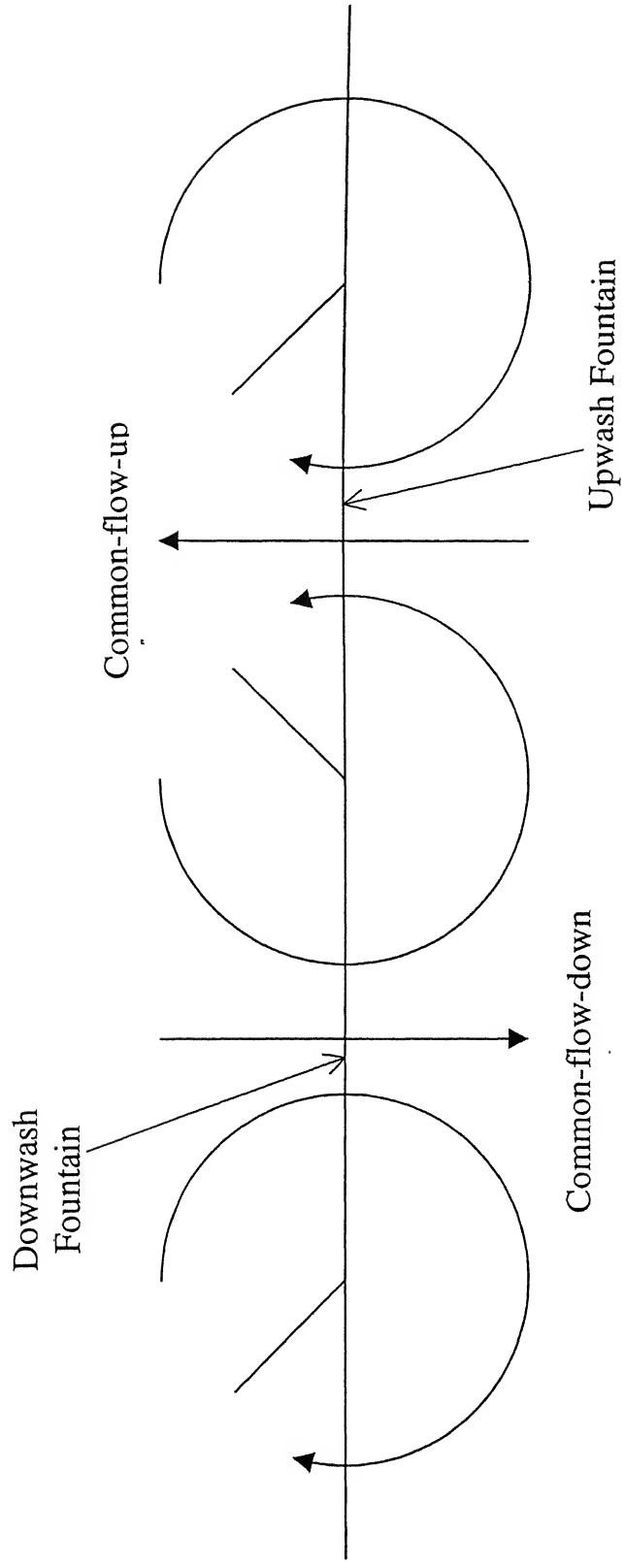


Figure 5.11 Flow structure due to delta winglets

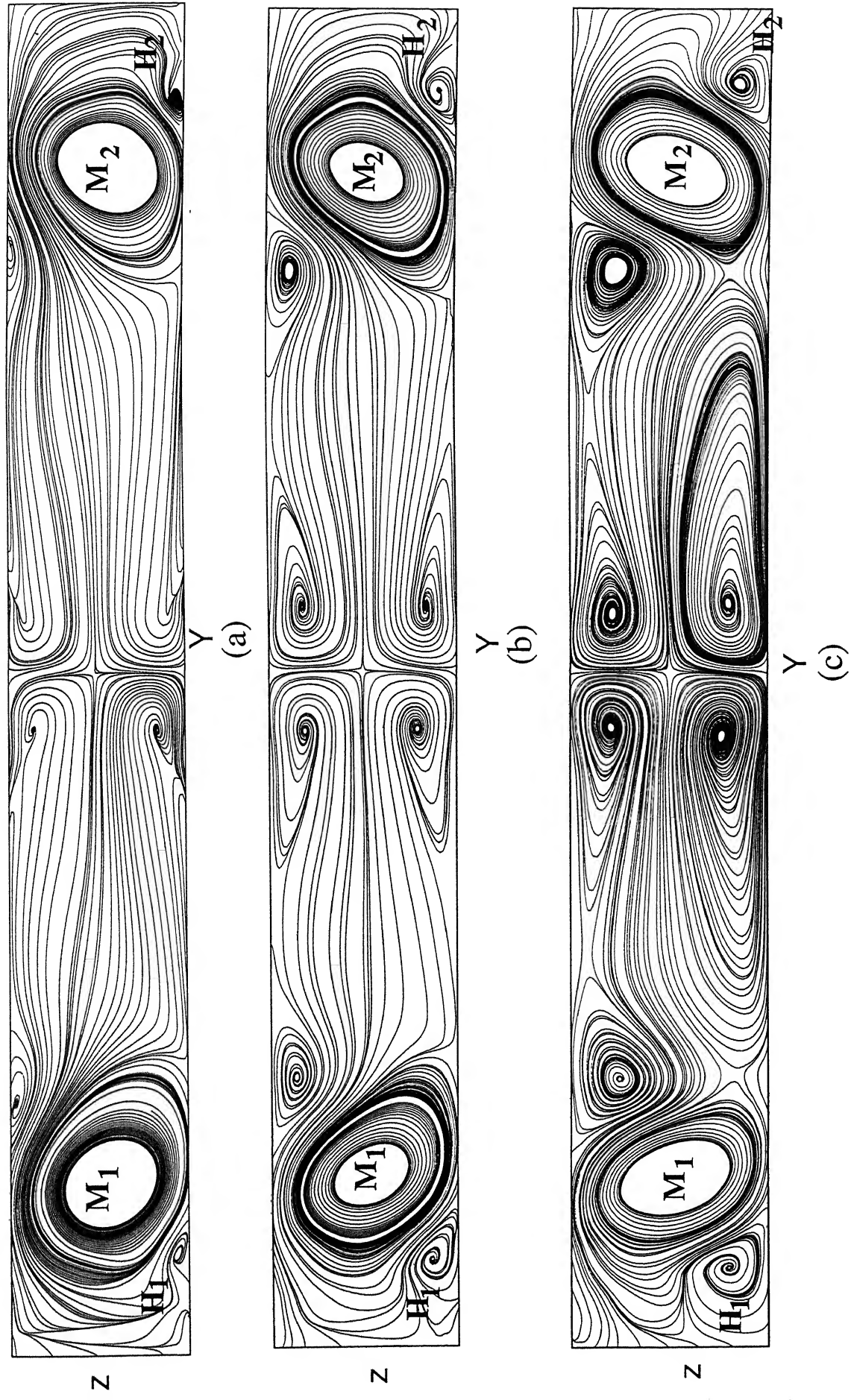


Figure 5.12 Streamline plot in cross plane at various X locations

(a) $X = 11$, (b) $X = 16$, (c) $X = 21$

centers of main vortices are located at a distance of $\pm 0.3B$ from the vertical mid plane. Induced vortices become prominent as the pair of longitudinal vortices travel in the downstream

5.4 Heat Transfer Characteristics in Plane Channel with Built-in Circular Tube and Winglet Pair

Figure 5.13 compares span-averaged Nusselt number distribution on the bottom wall in a channel for the case of built-in circular tube, with and without winglet pair. The Nusselt number distribution starts with a high value and decreases in the flow direction due to the growth of boundary layer on the bottom plate. The Nusselt number assumes a high value near the axial location of the leading edge of the circular tube. As the fluid approaches the stagnation line of the circular tube, it slows down and its pressure increases. The smaller velocity within the boundary layer in the vicinity of the bottom plate, which supports the circular tube, leads to a smaller pressure increase. Thus the induced pressure gradient causes a downward flow towards the bottom wall. Having impinged on the plate, the fluid rolls up forming vortices which finally wrap around the front half of the tube and extends to the rear of the tube (Goldstein and Karni(1984)). The resulting motion can be best described as a horseshoe vortex system. The horseshoe vortices are also longitudinal vortices and they promote disruption of thermal boundary layer. The Nusselt number is enhanced due to the horseshoe vortices.

An abrupt increase of Nusselt number is observed near the axial location of trailing edges of the winglet pair. Two counter-rotating longitudinal vortices culminate during creation of a complex vortex system due to the winglet pair. The formation of longitudinal vortices brings about better mixing and the Nusselt number becomes high near the location of the winglets. The span-averaged Nusselt number reaches a high value (9.31) near the axial location of the leading edge of the circular tube. This is primarily governed by the

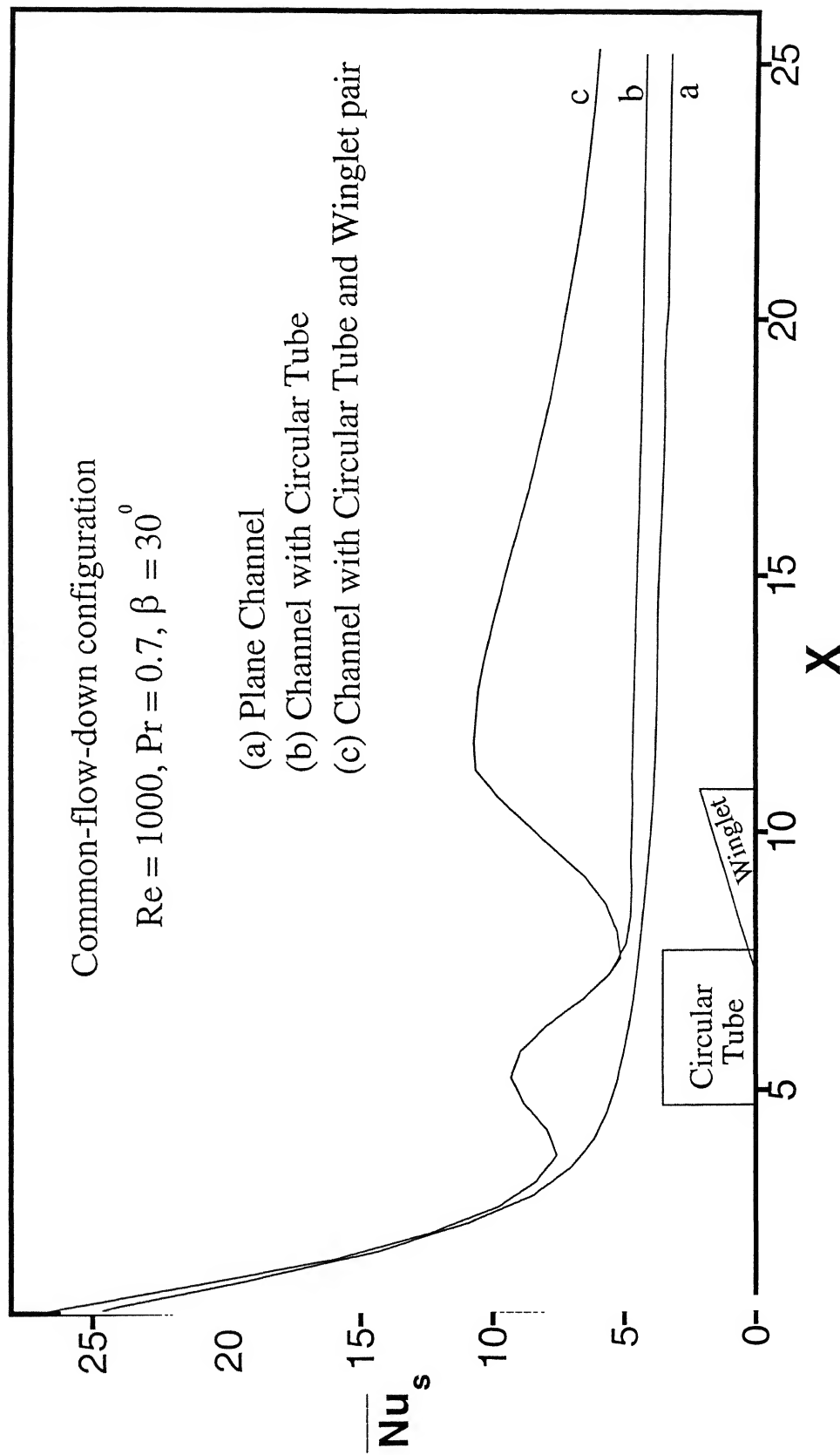


Figure 5.13 \overline{Nu}_s for plane channel, channel with circular tube and channel with circular tube and winglet pair

formation of the horseshoe vortices at the tube and bottom wall junction as explained earlier. Up to the location of the leading edge of the winglet pair, the distribution of span-averaged Nusselt number is same for the cases with and without winglet pair. However, beyond that location span-averaged Nusselt number increases for the case of channel with the tube and winglet pair. The peak value of span averaged Nusselt number takes place in the neighborhood of the trailing edge ($x=10.5$) of the winglet pair and its value is 10.74. The maximum enhancement in heat transfer (230%) is also observed at the same location. At the exit of the channel, the span-averaged Nusselt number is 6.03. The span-averaged Nusselt number at the exit of the plane channel is 3.26. The average Nusselt number value of the entire bottom plate for the case of a channel with built-in circular tube and the winglet pair is 40 percent more than that for the case of a channel with a built-in circular tube.

Iso-Nusselt number plot on bottom plate is shown in Figure 5.14. From entry till the end of the circular tube, the variation of Nu is similar to that in Figure 5.6. In Figure 5.14 winglets are placed at locations W_1 and W_2 . Figure shows increase in Nusselt number just after the location of winglet pair.

Figure 5.15 shows the distribution of local Nusselt number along the width of the channel at an axial location of $x=11$. This location is in the immediate downstream of the trailing edge of the winglet pair. The flow field and the temperature field used for calculation of local Nusselt number are at any arbitrary time instant. The peaks ($Nu = 19.2$) reconcile the effect of counter rotating longitudinal vortex pair. Maxima of the local Nusselt number occur at the spanwise locations where the downwash due to vortical motions impinges on the bottom plate.

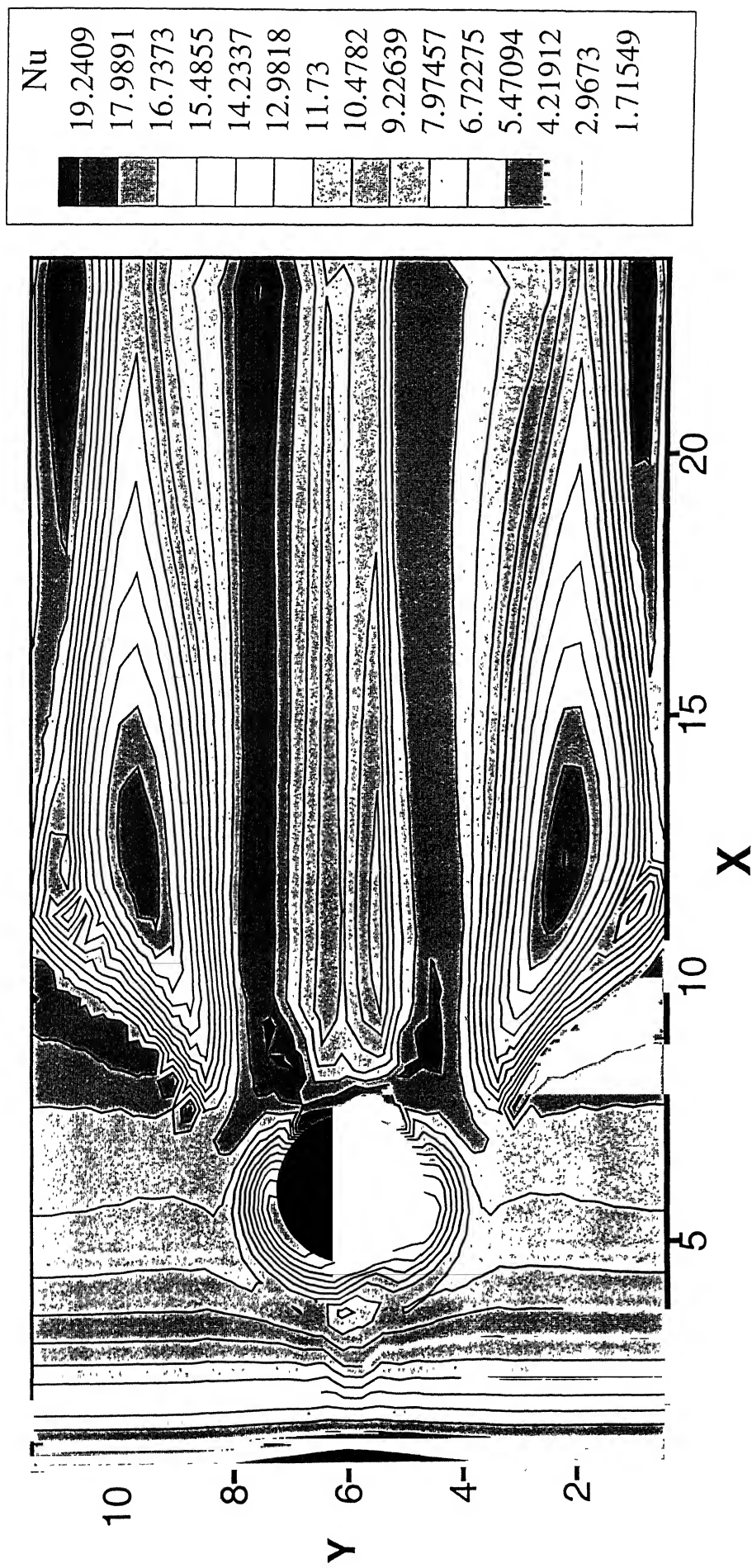


Figure 5.14 Iso-Nusselt number plot on the bottom plate

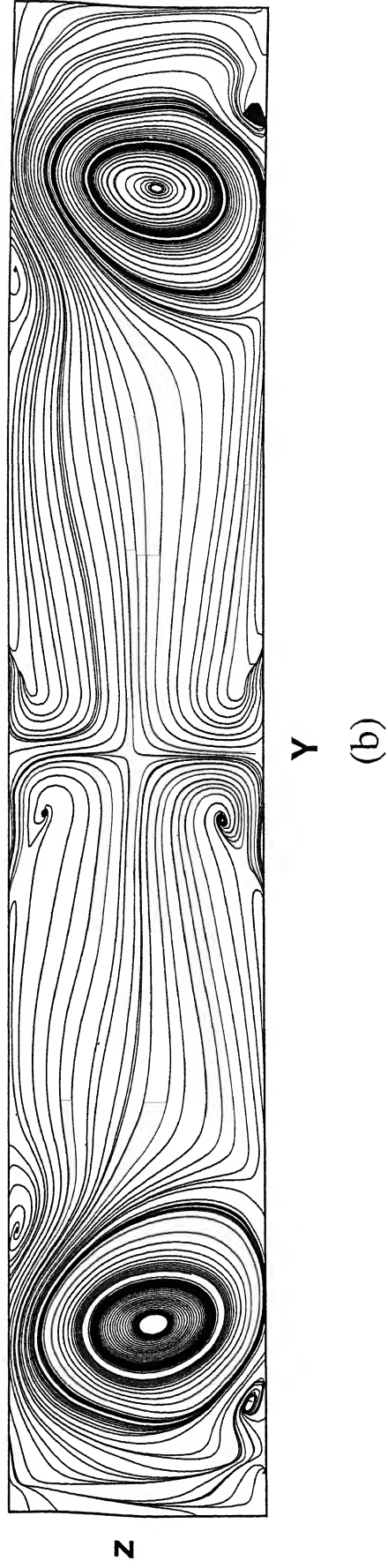
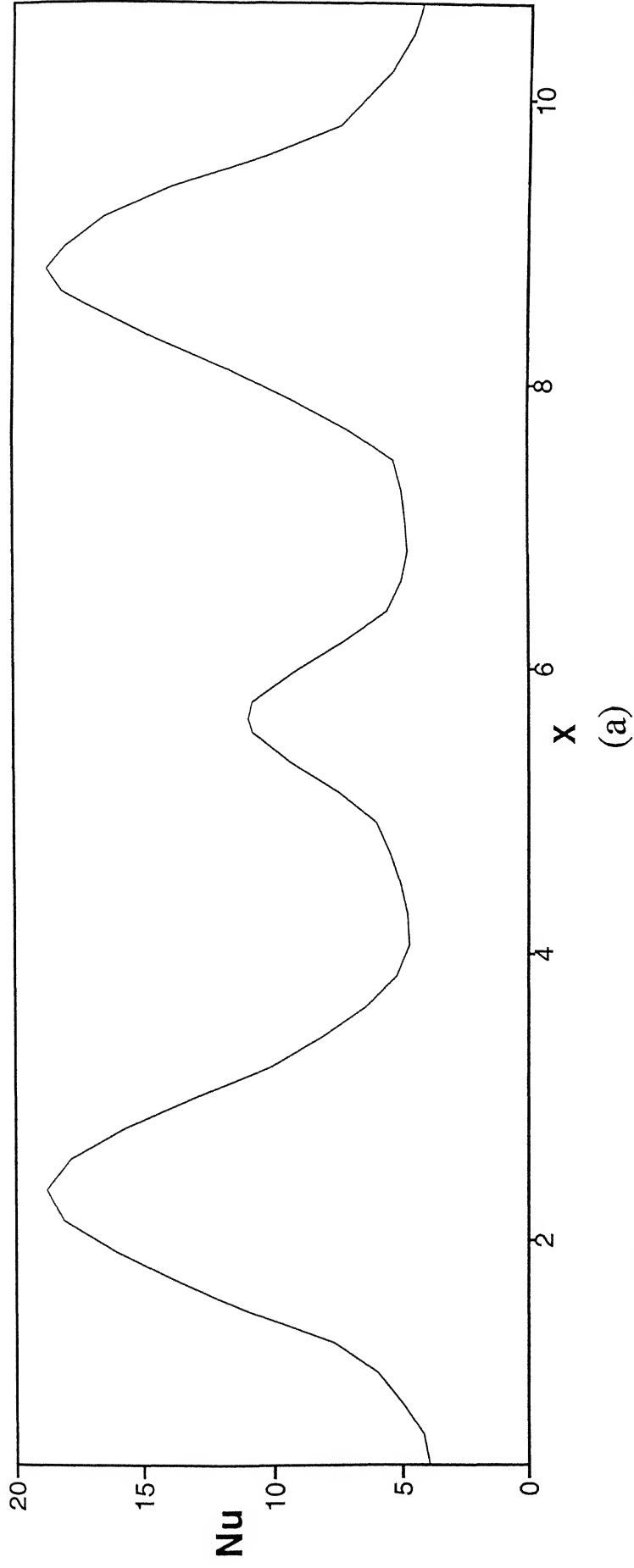


Figure 5.15 (a) Span-wise variation of Nusselt number at $X = 11$
(b) Streamlines in cross plane at the same location

5.5 Effect of Reynolds number and Angle of Attack on Heat Transfer

Figure 5.16 compares the variation of span averaged Nusselt number for a Reynolds number 1000 and at different angles of attack. The span-averaged Nusselt number ceases to be a strong function of the angle of attack of the winglet pair beyond $\beta = 24^\circ$.

Variation of \overline{Nu}_s for various Reynolds numbers at same angle of attack is shown in figure 5.17. It shows that \overline{Nu}_s increases with Reynolds number. For plane channel, it is known that \overline{Nu}_s increases with increase in Re. So even for the case of circular tube with winglet pair the correlations may still show increase of \overline{Nu}_s with Re (as it is observed here) but their exact nature needs further investigation.

5.6 Model Validation

The model validation was performed through comparison with the experimental results of Eckert and Soehngen (1952) and numerical results of Chun and Boehm (1989) for a Reynolds number of 200. Figure 5.18 shows the comparison of local Nusselt numbers along the circumference of the tube. Present computation compares favorably with the experiments of Eckert and Soehngen (1952).

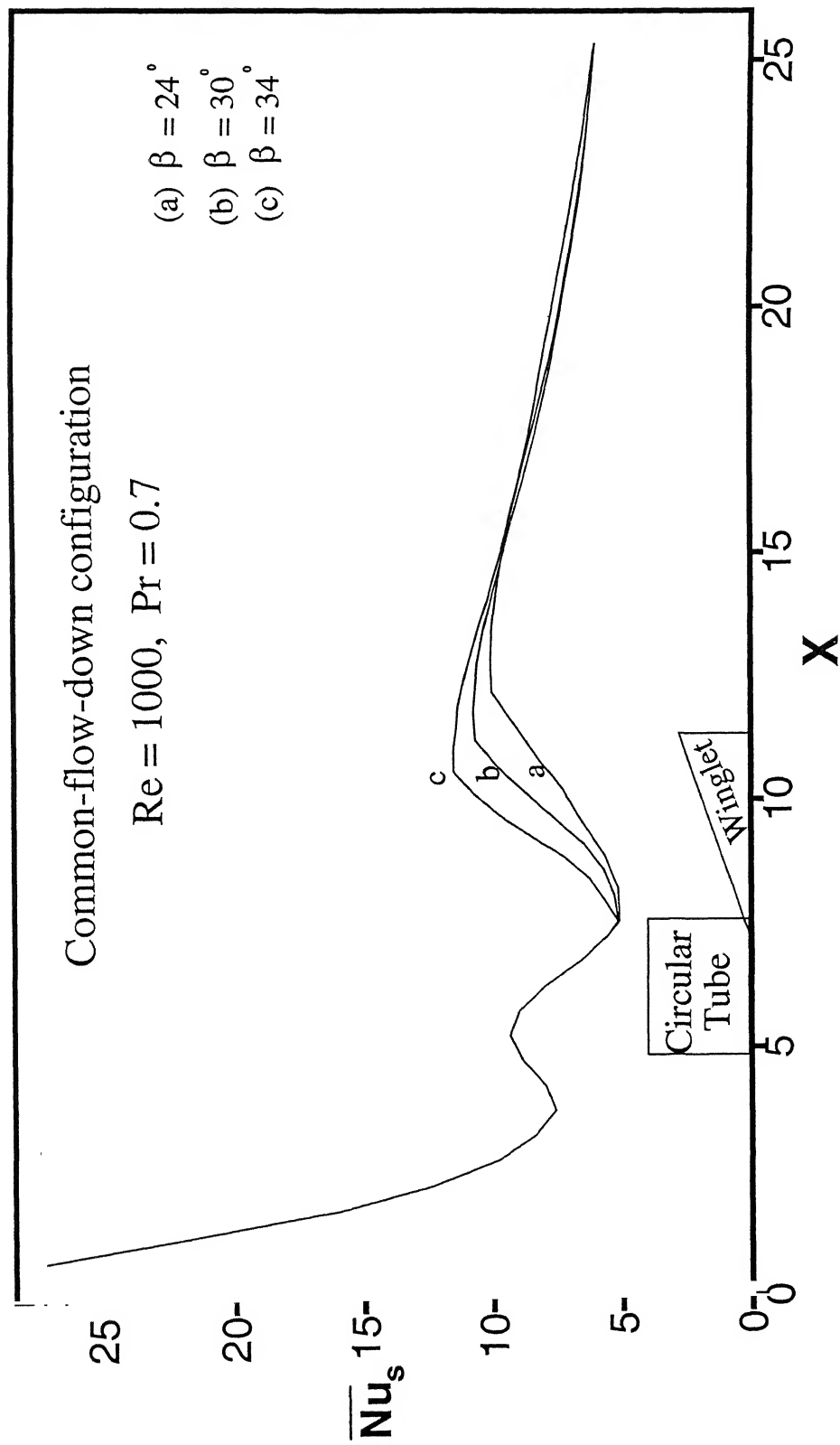


Figure 5.16 Variation of \overline{Nu}_s with the angle of attack (β)

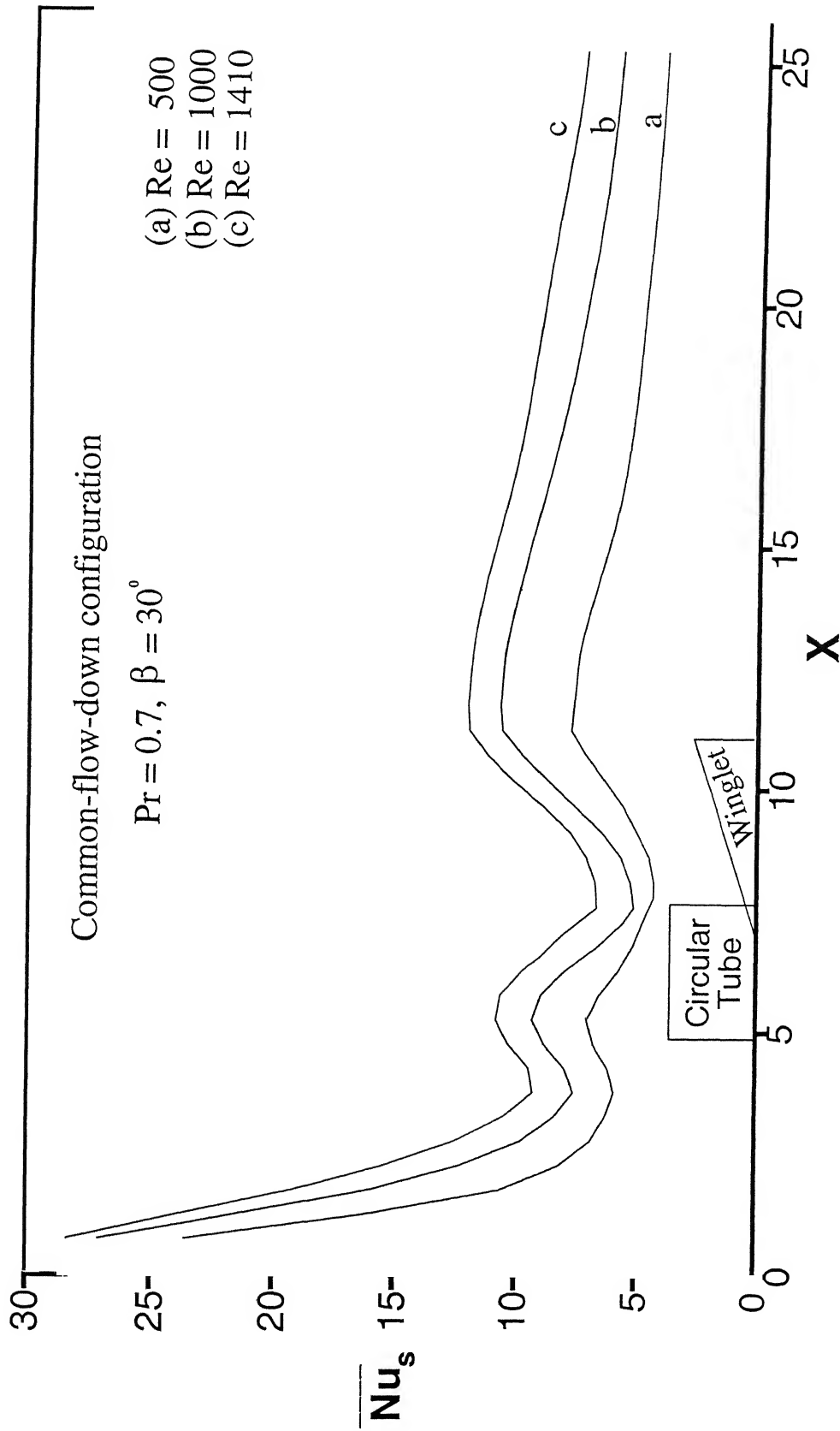


Figure 5.17 Variation of \overline{Nu}_s with Reynolds number (Re)

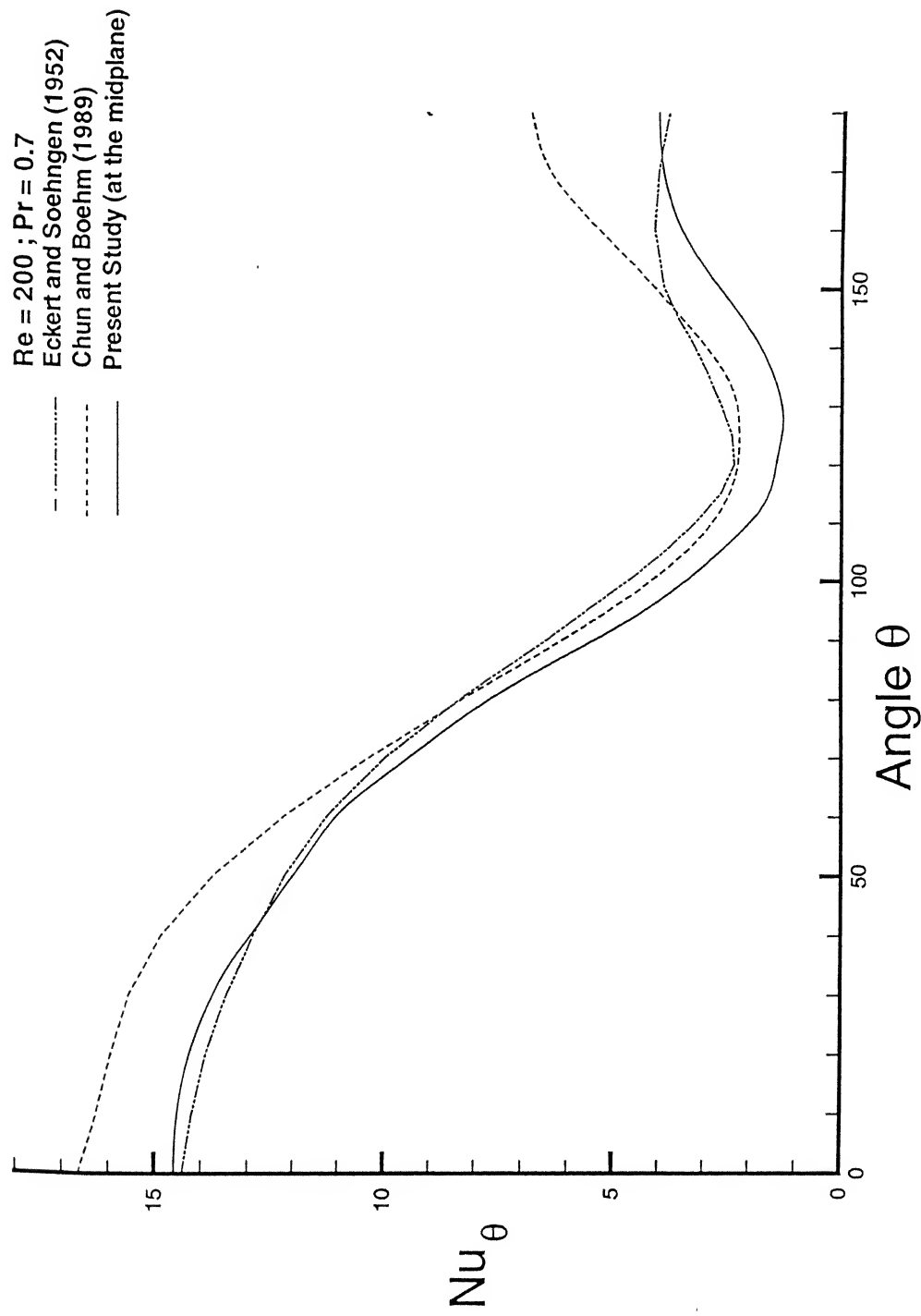


Figure 5.18 Comparison of local Nusselt number distribution on the Tube Surface

6 CONCLUSION AND SCOPE FOR FUTURE WORK

6.1 Conclusion

A three dimensional numerical study on the flow and heat transfer characteristics in plane channel with built-in circular tube and winglet pair in cross flow of the tube has been conducted. The delta winglet pair has been placed here in *common flow down* configuration. The duct was designed to simulate a passage formed by two neighboring fins in a fin-tube heat exchanger. The governing conservation equations of fluid flow are derived in integral form. An explicit control volume formulation devised by Eswaran and Prakash (1998) is used to solve the equations. A body fitting grid has been used for simulation of flow and heat transfer and investigation has been carried out for full domain. In computations of Biswas et al. (1994) the consideration of half domain for computation imposes a symmetry about vertical mid plane. This leads to suppression of possible vortex shedding. In present case of full domain computation, any chance of vortex shedding fully persists.

The streamline plot near the bottom wall clearly indicates the three-dimensionality of flow field, where all nodal points of attachment and saddle points of separation can be seen. The strength of longitudinal vortices beyond delta winglet pair is observed in cross plane and is seen to decrease in downstream direction. The consequence of this variation of vortical strength is reflected in decrease of span-averaged Nusselt number. The distribution of \overline{Nu} and iso-Nusselt number shows the high heat transfer zone behind the tube and beyond the trailing edge of winglet pair. This is the poor heat transfer zone due to presence of dead water wake zone behind the tube (Basu et al. 2000) in absence of winglet pair.

Delta winglet type vortex generators, placed in the aft of the circular tube, cause separation delay. This brings about narrowing of the wake and induces a strong swirling motion. The characteristic feature of the swirling motion is appearance of counter-rotating

vortical structures on the cross-stream planes behind the circular tube. The counter-rotating motion takes the cooler fluid from the underside of the core of the vortices, swirls around to upper side, entraining warmer fluid from the outside into the core of the vortices. As a result, the core region gets heated up and at the same time the heat transfer from the wall to the fluid is enhanced due to disruption of thermal boundary layer. Thus the zone of poor heat transfer from the near wake of the circular tube is removed. The creation of streamwise longitudinal vortices entail 230 percent enhancement of span-averaged Nusselt number in the near wake. The augmentation of average Nusselt number on the bottom plate is about 40 percent.

6.2 Scope for Future Work

The results of this work validate the unsteady flow modes as a useful technique in improving heat transfer efficiency for air-cooled heat exchangers. Similar to the common flow down configuration analyzed here the case of common flow up configuration could also be taken up and a comparison made with present results. The latter case will have leading edges of winglets more separated than trailing edges. One thing is obviously expected that latter case will reduce the wake zone significantly. But the behavior of Nu variation etc. is still a question. Also the circular tube could be replaced by oval tube and delta winglet pair to be mounted in the aft of the tube and results compared with present case. Even more than a pair of delta winglets could be mounted. In all these case delta winglet pair could well be replaced by rectangular winglet pair and the results compared.

Also the variation of vortical strength with downstream distance beyond winglet pair could be investigated and its correlation with \overline{Nu} could be confirmed. Establishing optimum angle of attack for these cases is still a potential problem to be tackled.

REFERENCES

1. Achaichia, A. and Cowell, T. W. (1988), Heat Transfer and Pressure Drop Characteristics of Flat Tube and Louvered Plate Fin Surfaces, *Experimental Thermal and Fluid Science*, Vol. 1, pp 147-157.
2. Acharya, S., Myrum, T. A. and Inamdar, S. (1991), Sub-harmonic Excitation of the Shear layer between Two Ribs: Vortex Interaction and Pressure Field, *AIAA J.*, Vol. 29, pp. 1390-1399.
3. Amon, C.H. and Patera, A.T. (1989), Numerical Calculation of Stable Three-Dimensional Tertiary States in Grooved-Channel Flow, *The Physics of Fluids-A*, Vol. 35, pp. 803-814.
4. Basu, S., Eswaran, V. and Biswas, G. (2001), Numerical prediction of Flow and Heat Transfer in a Rectangular Channel with a Built-in Circular Tube, *Proceedings of IMECE*, New York City, USA.
5. Biswas, G. and Chattopadhyay, H. (1992), Heat Transfer in a Channel with Built-in Wing-type Vortex Generators, *Int. J. Heat And Mass Transfer*, Vol. 35, pp. 803-814.
6. Biswas, G. and Mitra, N.K. (1998), Longitudinal Vortex Generators for Enhancement of Heat Transfer in Heat Exchanger Applications, *Proc. 11th Int. Heat Transfer Conference*, Kyongju, Vol. 5, pp. 339-344.
7. Biswas, G., and Mitra, N.K. and Fiebig, M. (1994), Heat Transfer enhancement in Fin-Tube Heat Exchangers by Winglet-Type Vortex Generators, *Int. J. Heat and Mass Transfer*, Vol.35, pp. 803-814.

8. Biswas, G., Torii, K., Fujii, D. and Nishino, K. (1996), Numerical and experimental determination of flow structure and heat transfer effects of longitudinal vortices in a channel flow, *Int. J. Heat Mass Transfer*, Vol. 39, No. 16, pp. 3441-3451.
9. Blomerius, H. and Mitra, N. K. (2000), Numerical investigation of convective heat transfer and pressure drop in wavy ducts, *Numerical Heat Transfer, Part A*, Vol. 37, pp. 37-54.
10. Braza, M., Chassaing, P. and Ha-Minah, H. (1986), Numerical Study and Physical analysis of the Pressure and Velocity Fields in the Near Wake of a Circular Cylinder, *J. Fluid Mechanics*, Vol. 165, pp. 79-130.
11. Brockmeier, U., Fiebig, M., Guntermann, T. and Mitra, N. K. (1989), Heat transfer enhancement in fin-plate heat exchangers by wing type vortex generators, *Chem. Engg. Technol.*, Vol. 12, pp. 288-294.
12. Chorin, A. J. (1967), A Numerical Method for Solving Incompressible Viscous Flow Problems, *J. Comp. Physics*, Vol. 2, pp. 12-26.
13. Chun, W. and Boehm, R. F. (1989), Calculation of forced flow and heat transfer around a cylinder in cross flow, *Numerical Heat Transfer*, Vol. 15, pp. 105-122.
14. Deb, P., Biswas, G. and Mitra, N. K. (1995), Heat transfer and flow structure in laminar and turbulent flows in a rectangular channel with longitudinal vortices, *Int. J. Heat Mass Transfer*, Vol. 38, pp. 2427-2444.
15. Dong, Y. (1989), Experimentelle Untersuchung der Wechselwirkung von Langswirbel-erzeugern und reiszylindern in Bezug auf Wärmeübergang und Strömungsverlust, Doctoral Thesis, Ruhr-Universität Bochum, Germany.

16. Eckert, E. R. G. and Soehngen, E. (1952), Distribution of Heat transfer coefficients around circular cylinders in cross flow at Reynolds numbers from 20-500, *Trans. ASME*, Vol. 74, pp.343-347.
17. Eibeck, P.A. and Eaton, J.K. (1986), Heat Transfer Effects of a Longitudinal Vortex Embedded in a Turbulent Shear Flow, *Journal of Heat Transfer*, Vol. 109, pp. 16-24.
18. Eswaran, V. and Prakash, S. (1998), A finite volume method for Navier-Stokes equations, *Proceedings of the Third Asian CFD Conference, Bangalore*, Vol. 1, pp. 251-269.
19. Ferziger, J. H. and Peric, M. (1999), *Computational Methods for Fluid Dynamics*, Springer Verlag, Berlin, Germany.
20. Fiebig, M., Kallweit, P. and Mitra, N. K. (1986), Wingtype Vortex Generators for Heat Transfer Enhancement, *Proceedings of the Eighth International Heat Transfer Conference*, San Fransico, Vol. 6, pp. 2909-2913.
21. Fiebig, M., Brockmeier, U., Mitra, N. K. and Guntermann, T. (1989), Structure of velocity and temperature fields in laminar channel flows with longitudinal vortex generators, *Numerical Heat Transfer, Part A*, Vol. 15, pp. 281-302.
22. Fiebig, M., Dong, Y. and Mitra N.K. (1990), Wärmeübergangserhöhung und Widerstandsverringern durch Längswirbelerzeuger in Rippenrohren, *Warme und Stoffübertragung*, Vol. 25, pp. 34-44.
23. Fiebig, M., Kallweit, P., Mitra, N. K. and Tiggelbeck, S. (1991), Heat Transfer Enhancement and Drag by Longitudinal Vortex Generators in Channel Flow, *Experimental Thermal and Fluid Science*, Vol. 4, pp. 103-114.
24. Garg, V. K. and Maji, P. K. (1987), Flow through a Converging-Diverging Tube with Constant Wall Enthalpy, *Numerical Heat Transfer*, Vol. 12, pp. 285-305.

25. Ghaddar, N. K., Korczak, K. Z., Mikic, B. B. and Patera, A. T. (1986), Numerical Investigation of Incompressible Flow in Grooved Channels, Part 2, Stability and Self-sustained Oscillations, *J. Fluid Mech.*, Vol. 163, pp. 99-127.
26. Goldstein, R. J. and Karni, J. (1984), The effect of a wall boundary layer on a local mass transfer from a cylinder in crossflow, *Journal of Heat Transfer (ASME)*, Vol. 106, pp. 260-267.
27. Harlow, F. H. and Welch, J. E. (1965), Numerical calculation of time-independent viscous incompressible flow of fluid with free surface, *The Phys. Fluids*, Vol. 8, pp. 2182-2188.
28. Hirt, C. W. and Cook, J. L. (1972), Calculating Three-Dimensional Flows around Structures and over Rough Terrain, *J. Comp. Phys.*, Vol. 10, pp.324-340.
29. Hummel, D. (1973), Study of the Flow Around Sharp-Edges Slender delta wings with Large Angles of Attack, NASA TTF-15, Vol. 107.
30. Hummel, D. and Srinivasan, P. S. (1967), Vortex Breakdown Efforts on the Low-speed Aerodynamic Characteristics of Delta Wings in Symmetrical Flow, *J. Roy. Aero. Soc.*, Vol. 71, pp. 66-82.
31. Kaul, U. K., Kwak, D., and Wagner, C. (1985), Computational Study of Saddle Point Separation and Horseshoe Vortex System, *AIAA J.*, Paper85-0812, Reno, Nev.
32. Kim, S. W. and Bnson, T. J. (1992), Comparison of SMAC, PISO and Iterative Time-Advancing Schemes for Unsteady Flows, *Computers and Fluids*, Vol. 21, pp. 435-454.
33. Kobayashi, M. H. and Pereira, C. F. (1991), Calculation of Incompressible Laminar Flows on a Non-Staggered, Non-Orthogonal Grid, *Numerical Heat Transfer*, Part B, Vol. 19, pp. 243-262.

34. Majumdar, S. (1998), Role of underrelaxation in momentum interpolation for calculation of flow with nonstaggered grids, *Numerical Heat Transfer*, Vol. 13, pp. 125-132.
35. Mendez, R. R., Sen, M., Yang, K. T. and McClain, R. L. (1998), Enhancement of heat transfer in an inviscid-flow thermal boundary layer due to a Rankine Vortex, *Int. J. Heat Mass Transfer*, Vol. 41, pp. 3829-3840.
36. Mukhopadhyay, A., Sundarajan, T. and Biswas, G. (1993), An Explicit Transient Algorithm for Predicting Incompressible Viscous Flows in Arbitrary Geometry, *Int. J. Numerical Methods Fluids*, Vol. 17, pp. 975-993.
37. Myrum, T. A., Acharya, S., Inamdar, S., and Mehrotra, A. (1992), Vortex Generators Induced Heat Transfer Augmentation Past a Rib in a Heated Duct Air Flow, *Journal of Heat Transfer*, Vol. 114, pp. 280-284.
38. Orlanski, I. (1976), A Simple Boundary Condition for Unbounded flows, *J. Comp. Phys.*, Vol. 21, pp. 251-269.
39. Patankar, S. V. and Spalding, D. B. (1972), A Calculation Procedure for Heat Mass and Momentum Transfer in Three-Dimensional Parabolic Flows, *Int. J. Heat Mass Transfer*, Vol. 15, pp. 1787-1806.
40. Patankar, S. V. (1981), A Calculation Procedure for Heat Mass and Momentum Transfer in Three-Dimensional Parabolic Flows, *Int. J. Heat Mass Transfer*, Vol. 15, pp. 1787-1806.
41. Peric, M. (1985), A Finite Volume Method for the Prediction of Three-Dimensional Fluid Flow in Complex Ducts, Ph.D. Thesis, University of London.

42. Peric, M., Kessler, R. and Scheuerer, G. (1988), Comparison of finite-volume numerical methods with a Staggered and Collocated Grids, *Computer & Fluids*, Vol. 16, pp. 389-403.
43. Pauley, W. R. and Eaton, J. K. (1988), Experimental study of the development of longitudinal vortex pairs embedded in a turbulent boundary layer, *AIAA J.*, Vol. 26, pp. 816-823.
44. Rhie, C. M. (1981), A Numerical Study of the Flow Past an Isolated Airfoil with Separation, Ph. D. Thesis, Dept of Mechanical and Industrial Engineering, University of Illinois at Urbana Champaign.
45. Rhie, C. M. and Chow, B. L. (1983), Numerical study of flow past an aerofoil with trailing edge separation, *AIAA J.*, Vol. 21, pp. 1525-1532.
46. Sanchez, M., Mitra, N. K. and Fiebig, M. (1989), Numerical investigations of three-dimensional laminar flows in a channel with built-in circular cylinder wing-type vortex generators, Proc. Eighth GAMM-Conference on numerical methods, Vieweg Verlag, pp. 484-492.
47. Sohankar, A. Davidson, L. and Norberg, C. (1999), Simulation of Unsteady Three-Dimensional Flow around a Square Cylinder at Moderate Reynolds Numbers, *Phys. Fluids*, Vol. 11, No. 2, pp. 288-306.
48. Sohankar, A. Davidson, L. and Norberg, C. (2000), Large Eddy Simulation of Flow Past a Square Cylinder: Comparison of different Subgrid Scale Models, *Trans. ASME: J. Fluids Engrg.*, Vol. 122, No. 1, pp. 39-47.
49. Sohankar, A. and Davidson, L. (2001), Effect of inclined vortex generators on heat transfer enhancement in a three-dimensional channel, *Numerical Heat Transfer, Part A*, Vol. 39, pp. 433-448.

50. Tiggelbeck, S., Mitra, N. K. and Fiebig, M. (1992), Flow structure and heat transfer in a channel with multiple longitudinal vortex generators, *Exp. Thermal Fluid Sci.*, Vol. 5, pp. 425-436.
51. Tsai, S. F., Sheu, T. W. H. and Lee, S. M. (1999), Heat transfer in a conjugate heat exchanger with a wavy fin surface, *Int. J. Heat Mass Transfer*, Vol. 42, pp. 1735-1745.
52. Turk, A. J. and Junklan, G. H. (1986), Heat Transfer Enhancement Downstream of Vortex generators on a Flat Plate, *Proc. 8th IHTC*, Vol. 6, pp. 2903-2908, San Francisco.
53. Valenica, A (1992), Wärmeübergang und Druckverlust in Lamellen-Rohr-Wärmeübertragern mit Langswirbelerzeugern, Doctoral Thesis, Ruhr Universität, Bochum, Germany.
54. Valenica, A., Fiebig, M. and Mitra, N. K. (1996), Heat transfer enhancement by longitudinal vortices in fin-tube heat exchanger element with flat tubes, *Journal of Heat Transfer (ASME)*, Vol. 118, pp. 209-211.
55. Van Doormal, J, P, and Raithby, G. D. (1984), Enhancement of the SIMPLE method for Predicting Incompressible Fluid Flows, *Numerical Heat Transfer*, Vol. 7, pp. 147-163.
56. Vanka, S. P. (1987), Second-Order Upwind Differencing in a Recirculating Flow, *AIAA J.*, Vol. 17, pp. 1079-1096.
57. Velusamy, K. and Garg, V. K. (1993), Entrance Flow in Elliptic Ducts, *Int. J. Numerical Methods Fluids*, Vol. 17, pp. 1079-1096.
58. Vicelli, A. J. (1971), A Computing Method for Incompressible Flows Bounded by Moving Walls, *J. Comp. Phys.*, Vol. 8, pp. 119-143.

59. Webb, B. W. and Ramadhyani, S., (1985), Conjugate Heat Transfer in a Channel with Staggered Ribs, *Int. J. Heat Mass Transfer*, Vol. 28, pp. 1679-1687.
60. Yanagihara, J. L. and Torii, K., (1990), Heat Transfer characteristics of Laminar Boundary Layer in the Presence of Vortex generators, *Proceedings of the Ninth International Heat Transfer Conference*, Vol. 6, pp. 323-328.
61. Zhang., Fiebig, M. and Mitra, N. K. (1989), Vortex Breakdown on Heat Transfer Enhancement in Flows between Parallel Plates, Eurotherm Seminar No. 91, Heat Transfer in Single Phase Flows, Bochum, pp. 97-104.

A

141969



A141969